

This is the peer reviewed version of the following article:

Mineralizations and transition metal mobility driven by organic carbon during low-temperature serpentinization / Ménez, Bénédicte; Pasini, Valerio; Guyot, François; Benzerara, Karim; Bernard, Sylvain; Brunelli, Daniele. - In: LITHOS. - ISSN 0024-4937. - 323:(2018), pp. 262-276.
[10.1016/j.lithos.2018.07.022]

Terms of use:

The terms and conditions for the reuse of this version of the manuscript are specified in the publishing policy. For all terms of use and more information see the publisher's website.

07/05/2026 01:00

(Article begins on next page)

1 **Mineralizations and transition metal mobility driven by organic carbon during**
2 **low-temperature serpentinization**

3 Bénédicte Ménez ^{a,*}, Valerio Pasini ^{a,b,#}, Francois Guyot ^c, Karim Benzerara ^c, Sylvain Bernard ^c,
4 Daniele Brunelli ^{b,d}

5 ^a *Institut de Physique du Globe de Paris, Sorbonne Paris Cité, Univ. Paris Diderot, UMR CNRS 7154, 1 rue Jussieu,*
6 *75238 Paris cedex 05, France*

7 ^b *Dipartimento di Scienze Chimiche e Geologiche, Università di Modena e Reggio Emilia, Via Campi 103, 41125*
8 *Modena, Italy*

9 ^c *Sorbonne Université, Muséum National d'Histoire Naturelle, UMR CNRS 7590, IRD, Institut de Minéralogie, de*
10 *Physique des Matériaux et de Cosmochimie, 4 place Jussieu, 75005 Paris, France*

11 ^d *Istituto di Scienze del Mare-CNR, Via Gobetti 101, 49100 Bologna, Italy*

12

13 * Corresponding author at: Institut de Physique du Globe de Paris, 1 rue Jussieu, 75238 Paris cedex
14 05, France

15 *E-mail address:* menez@ipgp.fr (B. Ménez)

16 # now at SRA Instruments SpA, Via Alla Castellana 3, 20063 Cernusco sul Naviglio, Italy

17

18 *Revised version Lithos – July 2018*

19

20 *Keywords:*

21 serpentinization

22 mid-ocean ridges

23 organic carbon

24 metal mobility

25 organomineralization

26 supergene ore formation

27

28 *Abbreviations:*

- 29 bast: bastite
- 30 C-XANES: X-ray absorption near edge structure at the carbon K-edge
- 31 EDXS: energy dispersive X-ray spectrometry
- 32 EMPA: electron microprobe analysis
- 33 EPS: extracellular polymeric substances
- 34 Fe-ox: iron oxide
- 35 FIB: focused ion beam
- 36 H-adr: andraditic hydrogarnet
- 37 HAADF-STEM: high-angle annular dark-field scanning transmission electron microscopy
- 38 HR-TEM: high resolution transmission electron microscopy
- 39 pol-spt: polygonal and polyhedral serpentine
- 40 SAED: selected area electron diffraction
- 41 SEM: scanning electron microscopy
- 42 spl: spinel
- 43 spt: serpentine
- 44 STEM: scanning transmission electron microscopy
- 45 STXM: scanning transmission X-ray microscopy
- 46 TEM: transmission electron microscopy
- 47

48 ABSTRACT

49 Serpentinization is known to provide substantial amounts of energy in the form of molecular
50 hydrogen along with a suite of abiotic organic compounds of low molecular weight (mainly as short
51 chain alkanes and carboxylic acids), all sustaining the development of microbial ecosystems in the
52 mantle-derived crust. The latter have a cryptoendolithic life style and are responsible for (i) the
53 local formation of biomass and of organic metabolic byproducts and (ii) the production of
54 extracellular polymeric substances which organize the community in the form of a biofilm at the
55 surface of the rock-forming minerals. In accordance, whatever their origin, organic compounds can
56 be diverse and widespread in the shallow oceanic crust where they undergo hydrothermal
57 degradation and remobilization through fluid circulations. Here we show that organic carbon is
58 directly involved in low temperature serpentinization reactions ($< 200^{\circ}\text{C}$). Fine scale investigations
59 of microbial niches hosted in serpentinites from the Mid-Atlantic ridge were performed using
60 scanning and transmission electron microscopy along with scanning transmission X-ray
61 microscopy. They suggest that organic films generated at mineral surfaces as a consequence of rock
62 colonization may influence the nature and structure of the serpentinization products as well as the
63 mobility and speciation of transition metals as the reaction progresses. This likely constitutes an
64 efficient yet poorly considered mechanism in active serpentinizing systems with possible
65 implications for ore formation associated with the alteration of ophiolitic massifs and subsurface
66 storage.

67

68 **1. Introduction**

69

70 It was long assumed that the net flux of most hydrothermally-derived metals to the ocean
71 was negligible because abundant polymetallic particulate phases, predominantly in the form of Fe-
72 sulfides and Fe-oxyhydroxides, form when vent fluids discharge at the seafloor (German et al.,
73 1991; Mottl and McConachy, 1990). Nonetheless, the importance of hydrothermally-derived metals
74 for ocean biogeochemistry has been revisited during the last two decades. Enrichments in dissolved

75 iron compared to predicted solubility values were reported in non-buoyant hydrothermal plumes,
76 suggesting that a fraction of metals escapes from precipitation (Field and Sherrell, 2000; Resing et
77 al., 2015; Statham et al., 2005). Organic compounds were shown to bind and stabilize dissolved
78 metals (Bennet et al., 2008; Hawkes et al., 2013; Sander and Koschinsky, 2011; Toner et al., 2009)
79 or solid sulfur and iron particles (Fitzsimmons et al., 2017; Klevenz et al., 2011; Lau and Hsu-Kim,
80 2008), overall facilitating their long-range oceanic transport (Fitzsimmons et al., 2017; Sander and
81 Koschinsky, 2011; Sands et al., 2012; Wu et al., 2011). Organic-metal complexation reduces the
82 reactivity of the metallic species and prevents metal redox changes, precipitation or scavenging into
83 or onto particulate phases (Bennett et al., 2008). Therefore, it significantly increases dissolved metal
84 concentrations in hydrothermal fluids and associated fluxes of metals to the global ocean (Resing et
85 al., 2015; Sander and Koschinsky, 2011). Although iron has been one of the most investigated
86 metals due to its role as a limiting nutrient (Bennet et al., 2008; Boyd and Ellwood, 2010; Sander
87 and Koschinsky, 2011; Toner et al., 2009), hydrothermally-derived chromium, copper, and
88 manganese have also been shown to be transported to the non-buoyant hydrothermal plume and
89 across oceans as complexes stabilized with organic ligands (Fitzsimmons et al., 2017; Resing et al.,
90 2015; Sander et al., 2007).

91 While their compositions and sources are not fully determined, these metal-stabilizing
92 organic complexes are postulated to form from organic ligands available in excess in the plume
93 source regions (Bennett et al., 2008, 2011). In addition to the small fraction of thermally-reworked
94 marine dissolved and particulate organic matter that outlived hydrothermal circulation (Hawkes et
95 al., 2015; Rossel et al., 2017) and organic compounds mobilized during hydrothermal alteration of
96 organic carbon-rich sediments (e.g., Kawka and Simoneit, 1987), these plume enrichments in
97 organic matter were postulated to derive from (i) chemosynthetic microbial activities occurring at or
98 close to vents (Lang et al., 2006), (ii) hydrothermal degradation of vent-hosted biological material
99 (Simoneit et al., 2004) and (iii) abiotic hydrothermal synthesis (Konn et al., 2015 and references
100 therein). All these processes form a large diversity of organic compounds pervasively entrained into
101 buoyant hydrothermal plumes through chimney venting or diffuse flow. However, life is not limited

102 to ocean, sediment or seafloor hydrothermal vent ecosystems and both the ultramafic and mafic
103 oceanic subseafloors were also recognized as potentially-large microbial habitats (Mason et al.,
104 2010; Ménez et al., 2012; Santelli et al., 2008). In particular, the serpentinization of mantle-derived
105 rocks is known to provide substantial amounts of molecular hydrogen through the reduction of
106 water coupled to the oxidation of ferrous iron-bearing minerals. This in turn favors the formation of
107 organic compounds such as short chain alkanes and carboxylic acids. Together with molecular
108 hydrogen, these organic compounds provide, despite the alkaline pHs associated with
109 serpentinization reactions, valuable energy sources for the development of cryptoendolithic
110 microbial ecosystems in the mantle-derived crust (Schrenk et al., 2013). These ecosystems can
111 locally form biomass and organic metabolic byproducts along with extracellular polymeric
112 substances (EPS) allowing to organize the community in the form of a biofilm at the surface of the
113 rock-forming minerals. Abiotic organic synthesis and biological metabolic activities thus coexist in
114 these environments, the complex interplay between both pathways during the multistage
115 hydrothermal alteration of the oceanic crust being however far from being understood. In
116 accordance, organic compounds can be diverse in origin and nature and pervasively present in the
117 shallow oceanic crust where they undergo hydrothermal degradation and remobilization through
118 fluid circulations (Pasini et al., 2013). Serpentinization reactions also affect redox-sensitive
119 transition metals resulting in the formation of oxides, sulfides, native elements and alloys,
120 depending on the chemical and physical conditions of the system. Organic complexation may also
121 impact the fate of metals at depth in the oceanic lithosphere and play a role during fluid-rock
122 interactions that has never been considered yet.

123 Ménez et al. (2012) provided evidence for cobalt enrichments associated with the presence
124 of carbon-rich phases in a serpentinite from the equatorial Mid-Atlantic Ridge (MAR). These
125 organic phases were inherited, at least partly, from the presence of former ecosystems identified
126 through remnants of complex organic molecules. The organic phases were also suggested to
127 mediate the formation of polygonal and polyhedral serpentines (pol-spt) precipitating in the cavities
128 of andraditic hydrogarnets (H-adr). Overall, this suggested a potential role of organic compounds in

129 the regulation of elemental fluxes in the serpentinizing oceanic lithosphere. Here, we further
130 investigate the occurrences of polyhedral and polygonal serpentine along with organic-metal
131 associations in this MAR serpentinite by using a suite of high-resolution techniques, which includes
132 electron microprobe analysis (EMPA), scanning and transmission electron microscopies (SEM and
133 TEM) coupled with energy dispersive X-ray spectrometry (EDXS), scanning transmission electron
134 microscopy (STEM), and scanning transmission X-ray microscopy (STXM) associated with X-ray
135 absorption near edge structure at the carbon K-edge (C-XANES). The spatially-resolved
136 characterization of transition metals and organic carbon down to the nanometer scale highlights (i)
137 the involvement of an organic gel in the formation of pol-spt, (ii) a differential distribution of
138 metals depending on the nature of the associated organic phases and (iii) the precipitation of
139 nanometer-sized metallic oxides within the organic phases.

140

141 **2. Material and methods**

142

143 *2.1. Geological setting*

144

145 The studied rock was dredged during the joint Russian-Italian cruise S22 (*R/V Akademik*
146 *Nikolaj Strakhov*) in the vicinity of the Sierra Leone area, a magma starved, slow-spreading region
147 of the equatorial MAR at 5-7° N (Figs. 1a-b). The non-transform Sierra Leone fault is located
148 between the Bogdanov and the Strakhov fracture zones (7°10' N and 4° N, respectively). The rift
149 zone is morphologically characterized by isolated basins, tectonically separated by transverse uplifts
150 (3000-2100 meters below seafloor) made up by outcrops of tectonized and altered deep-seated
151 gabbros and mantle rocks (Peyve et al., 2003; Sharkov et al., 2012). Sample S2232-17 was collected
152 on one of the most elevated blocks during the dredge haul S2232, which was carried out on an
153 unsedimented ridge flanks of crust aged < 1 My (dredging interval: 6°08.9' N-33°25.4' W-6°09.1'
154 N-33°25.4' from 2250 to 2000 meters below seafloor). About 200 kg of variably serpentinized
155 peridotites were recovered during this haul (Peive et al., 2003).

156

157 *2.2. Sample petrography*

158

159 The studied rock corresponds to a fully serpentinized peridotite similar to rocks usually
160 found in serpentinized mantle along Mid-Ocean ridges. Primary mineralogy has been tentatively
161 inferred on the basis of the isomorphic mineral substitution. Prior to serpentinization, the rock
162 primarily consisted in olivine + orthopyroxene + clinopyroxene + chromian-aluminous spinel
163 revealing a spinel field equilibrated harzburgite (with theoretical modal clinopyroxene < 1%). Only
164 few relics of those primary minerals can be found. They include clinopyroxenes, partially-preserved
165 chromite cores derived from the chromian-aluminous spinel and rare olivine kernels (Pasini, 2013).
166 As shown in Fig. 1c, the high temperature (> 200°C; Klein et al., 2014) hydrated paragenesis is
167 composed of lizardite and magnetite, both after olivine, forming a characteristic mesh texture.
168 Serpentine after olivine is also found around spinel remnants. Fine-grained lizardite, commonly
169 defined as bastite, pseudomorphically replaces orthopyroxene. Chains or clusters of subhedral
170 microgeode-like andraditic hydrogarnets (10-40 µm in size) are crystallized in, or very close to, the
171 bastitized orthopyroxene along exsolution lamellae or microfractures (Fig. 1d). They are locally
172 stretched or, alternatively, coalesce with one another and are often associated with iron oxides. H-
173 adr are commonly found in serpentinites and usually grow over bastite under high pH and high Ca²⁺
174 activity, low O₂ fugacity, low silica activity and temperature below 200°C (Frost and Beard, 2007
175 and references therein; Plümper et al., 2014). Late serpentine veins of millimeter widths crosscut
176 the whole rock, attesting for several stages of serpentinization (Fig. 1c).

177

178 *2.3. Sample preparation*

179

180 Conventional petrographic thin sections were prepared for EMPA. SEM observations were
181 performed on both silicon carbide-polished and unpolished, resin-free chips of sawn rock. TEM and
182 STXM require electron and X-ray transparent samples, respectively, i.e., measuring at least less

183 than ~100 nm in thickness. For this purpose, ultrathin focused ion beam (FIB) sections were milled
184 using the FIB dual beam facility FEI Strata DB 235 operating at the IEMN (Lille, France). Resin-
185 free chips were beforehand coated with gold in order to reinforce the protection of the surface and
186 limit ion implantation into the samples. Regions of interest were covered with a platinum strap and
187 then excavated from both side of the Pt strap using a 30 kV Ga⁺ beam, emitted from a Ga liquid
188 metal ion source operating at 7 to 1 nA. Further thinning to few tens of nanometers was obtained
189 with a glancing angle beam at low current (~100 pA). FIB foils have been repeatedly used to study
190 organic compounds within rocks with limited damages (e.g., Bassim et al., 2012; Benzerara et al.,
191 2005; Bernard et al., 2009; Lepot et al., 2009).

192

193 *2.4. Electron microscopy*

194

195 SEM observations were performed on Au-coated, polished and unpolished, resin-free chips
196 using a Zeiss SUPRA 55 VP field emission microscope (Service Commun de Microscopie
197 Electronique à Balayage, UPMC, Paris, France). Beam accelerating voltage ranged between 15 kV
198 (for backscattered electron images, microanalyses and chemical maps) and 1 kV (for high resolution
199 secondary electron images). Images were collected using secondary electron detectors (Everhart-
200 Thornley or InLens) and a backscattered electron detector (AsB). EDXS analyses were carried out
201 with a PGT Sahara spectrometer. Chemical maps were acquired and processed using the Spirit[®]
202 software. Spectra were fitted at each hyperspectral map point to produce elemental distributions.

203 TEM observations, high resolution-transmission electron microscopy (HR-TEM) and
204 selected area electron diffraction (SAED) were performed on ultrathin FIB sections using JEOL
205 2100 microscopes operating at an accelerating voltage of 200 kV (IMPIC, Paris, France and
206 Centro Interdipartimentale Grandi Strumenti, Modena, Italy). Both microscopes are equipped with a
207 LaB₆ filament. EDXS analyses were performed using a JEOL detector at IMPIC and an Oxford
208 INCA 100 detector at CIGS.

209 TEM images and STEM maps were also acquired on ultrathin FIB sections using a JEOL

210 2100F microscope equipped with a field effect gun and operating at 200 kV (IMPMC, Paris,
211 France). High-angle annular dark-field (HAADF)-STEM was used with a focused electron beam of
212 ~1 nm for Z-contrast imaging (Z referring to the atomic number). STEM-EDXS analyses were
213 performed using a JEOL detector equipped with an ultrathin window allowing the detection of low-
214 Z elements.

215 When necessary, SEM and TEM images were further processed with the ImageJ software
216 (Schneider et al., 2012) for contrast and brightness adjustment.

217

218 *2.5. Electron microprobe analysis*

219

220 EMPA were performed on carbon-coated petrographic thin sections using the Cameca
221 SXFive installed at CAMPARIS (Université Pierre et Marie Curie, Paris, France). Operating
222 conditions were 10 kV and ~10 nA. Analyses were acquired in punctual mode.

223

224 *2.6. Synchrotron-based scanning transmission X-ray microscopy*

225

226 STXM and associated C-XANES analyses were performed at the branch line 5.3.2.2
227 (STXM Polymer beamline; Kilcoyne et al., 2003) of the Advanced Light Source (Lawrence
228 Berkeley National Laboratory, USA). A zone plate was used to monochromatize and focus the X-
229 ray beam produced by the synchrotron radiation to a spot size of ~25 nm. The ultrathin FIB foils
230 were scanned in the x - y directions at fixed photon energy to produce 2D images. The x - y plane
231 refers to the plane perpendicular to the incident X-ray beam direction. The transmitted X-rays were
232 detected a few hundreds of microns behind the sample. Energy calibration was carried out using the
233 well-resolved peak of gaseous CO₂ at 294.96 eV. Carbon speciation maps with a 90 nm spatial
234 resolution were acquired under He atmosphere by collecting image stacks over the energy range
235 275-340 eV with a theoretical energy resolution of ~0.1 eV. Counting time was 1 ms per image.
236 The image contrast results from differential absorption of X-rays, which depends on the chemical

237 composition of the sample. Images stacks were aligned using two dimensional cross correlation and
238 processed using STACKLab, a Matlab[®] STXM data analysis script collection. This routine was also
239 used to process energy-filtered images and extract XANES spectra at the carbon K-edge in order to
240 document the bonding environment of carbon for the pixels of interest.

241

242 **3. Results**

243

244 *3.1. Polyhedral and polygonal serpentine formation from hydrogarnet dissolution mediated by an* 245 *organic gel*

246

247 Euhedral dissolution pits are often found as piercing the surface of the andraditic
248 hydrogarnets present in the S2232-17 serpentinite as shown by SEM (Fig. 2a) also highlighting
249 large cavities inside H-adr (Supplementary Fig. 1). This suggests that dissolution process affected
250 the hydrogarnets, as also proposed by Ménez et al. (2012). EMPA provided for H-adr a mean
251 formula of $\text{Ca}_{2.71}(\text{Fe}_{1.61}^{3+}, \text{Ti}_{0.01}, \text{Al}_{0.17}, \text{Cr}_{0.03}, \text{Mg}_{0.02})(\text{Si}_{2.92}\text{O}_{10.93})(\text{OH})_{1.07}$ (Supplementary Table 1).
252 Pits and cavities are filled by polyhedral serpentine spheroids and polygonal serpentine rods (pol-
253 spt), both showing a wide size range (few tens to 1,000 nm - mean 350 nm; Fig. 2c). Pol-spt show
254 an enrichment in Cr (mean 1.18 ± 0.89 wt.%) and to a lesser extent in Al (mean 4.32 ± 2.53 wt.%) and
255 Fe (mean 4.96 ± 0.91 wt.%) in comparison with the high temperature serpentines (i.e., the bastite,
256 the mesh serpentine and the serpentine contouring spinels) (Fig. 3, Supplementary Fig. 2 and
257 Supplementary Table 1). Conversely, the pol-spt display low concentrations in cobalt (0.07 ± 0.12
258 wt.%) and manganese (0.06 ± 0.08 wt.%) while nickel reaches concentrations similar to what was
259 found for the four other types of serpentine (0.22 ± 0.25 wt.%). When numerous, pol-spt appear to
260 fracture the H-adr crystals (Fig. 2b). This peculiar type of serpentine is also visible around the
261 hydrogarnets, filling various-sized voids around the H-adr spheroids (Figs. 2a, c and e), with a clear
262 indentation of the spheroids within the surrounding fine-grained bastite (Fig. 2f). H-adr crystals and
263 part of the bastite were progressively replaced by pol-spt that also spread inside the surrounding

264 remaining bastite through tiny veins (Figs. 2g-h).

265 The identification of pol-spt serpentines was confirmed by TEM and SAED (Figs. 4 and
266 5d). As described in literature (Baronnet and Devouard, 1996, 2005; Baronnet et al., 2007;
267 Andreani et al., 2008; Cressey et al., 2008, 2010), polyhedral serpentine is composed of triangular
268 facets made of lizardite basal planes showing lateral continuity from one sector to another and
269 forming tiny “onion like” geodesic spheroids (Fig. 4). The core of the spheroids usually hosts a
270 small fibre contoured by the triangular facets. Given that the geodesic spheroids have the simplest
271 formulation as icosahedra, the inner cavity is possibly defined by this geometric limit. Polygonal
272 serpentine crystallizes as tiny fibres composed of concentric lizardite layers wrapped around the
273 fibre axis and made of 15 or 30 sectors (Fig. 5d). The fifteen-sector fibres are the smallest (< 400
274 nm - mean 350 nm), whereas the thirty-sector ones are larger (up to 1,000 nm - mean 610 nm).

275 SEM and TEM analyses highlight a close connection between pol-spt and H-adr (Figs. 5a-
276 b). The globular topography of the H-adr inner cavities where pol-spt grew suggests local
277 transformation of H-adr into spherical and coalescent pol-spt (Fig. 5a). TEM analyses of FIB foils
278 milled on H-adr grains also show that the pol-spt enclosed in the branched and elongated
279 dissolution cavities are embedded in a carbon-rich phase also covering the H-adr walls (Figs. 5b, d-
280 g). This is in agreement with SEM observations collected on resin-free chips showing the presence
281 of carbon veils within the H-adr cavities (Fig. 5c). The organic film has a gel-like appearance and
282 does not show any structure or atomic organization using HR-TEM. It presents very low wetting
283 angles with respect to the phyllosilicate and the hydrogarnet (Figs. 5b and d). TEM-EDXS analyses
284 highlight the presence of Mg, Si and to a lesser extent, Ca and Fe in the gel (Fig. 5e), likely
285 responsible for the brightness of the fluffy phase observed by HAADF-STEM (Figs. 5f-g). The
286 organic nature of the carbon gel was further demonstrated by STXM coupled with C-XANES
287 spectroscopy. As displayed in Fig. 6e, the C-XANES spectrum of the carbon gel shows a major
288 peak at 288.6 eV, characteristic of carboxylic functional groups (Cody et al., 1998; Benzerara et al.,
289 2004; Bernard et al., 2009). STXM mapping shows that this organic phase is spectroscopically
290 homogeneous (Figs. 6d-e).

291

292 *3.2. Local enrichments in transition metals and associated carbon speciation*

293

294 Carbon-rich areas are also found as large patches in H-adr inner cracks and fractures nearby
295 iron oxides which precipitated concomitantly with H-adr (Fig. 7a). These carbon-rich patches are
296 associated with a complex intergrowth of late stage serpentines including pol-spt among numerous
297 nanometric to micrometric fibrous chrysotile-like aggregates (Figs. 7 and 8a). These felt-like
298 organic matter accumulations are associated with enrichments in transition metals, notably cobalt
299 (Fig. 8c; Ménez et al., 2012) but also manganese (Fig. 8b) and to a lesser extent iron and nickel
300 (Figs. 9e-h, 10 and 11). These metals are strictly confined to the H-adr filling material and not
301 dispersed in the host groundmass although some metal-rich nanophases can also be suspected in the
302 bastite and the mesh serpentine, based on EMPA (Supplementary Fig. 2 and Supplementary Table
303 1). With the exception of Fe, none of those elements were detected in the carbon gel embedding the
304 pol-spt previously described in the branched and elongated dissolution cavities (Figs. 5 and 6).

305 The felt presents an organic C-rich component with variable texture and porosity, finely
306 intermingled with various amounts of micro- to nano-crystallites. As an illustration, Fig. 9d (or
307 Supplementary Fig. 3 for an enlarged version of Fig. 9d) shows that polyhedral serpentine geodesic
308 spheroids and polygonal serpentines are embedded in a foamy carbon gel presenting a vesicular
309 texture with gradients in the size of the vesicles. The foamy appearance can be a primary character
310 or alternatively can have been induced by degassing of a light fraction or by cavitation under
311 vacuum during measurements. The significant decompression experienced during the recovery from
312 the seafloor can also be invoked. Variations of the texture seem however to be correlated with the
313 presence/absence of transition metals, the gel texture being locally more massive when the carbon
314 and metal contents are respectively lower and higher (Fig. 9). The foamy C-bearing gel is
315 associated with the presence of Co and minor Mn, Ni, and Fe (Figs. 9d, g and 11). In contrast, Fig.
316 9b shows a dense carbon-bearing phase spotted by subnanometric electron-dense phases that were
317 identified as well-crystallized Co-oxides (Figs. 10a-b and 11), likely responsible for the enrichment

318 in Co shown in Fig. 8c. In this area, Mn, Ni and Fe are also present in the C-phase but at lower
319 concentrations (Figs. 9e-f and 11). Similarly, a compact carbon-poor and likely more crystalline
320 matrix displaying high Mn concentrations was identified in the upper part of Fig. 9d
321 (Supplementary Fig. 3), based on STEM-EDXS mapping (Fig. 9h). In this area, pol-spt spheroids
322 are locally surrounded by well-crystallized Mn/Fe crusts measuring about 50 nm in thickness (Figs.
323 10c-d and 11). The surrounding C-bearing matrix also presents high Mn, and to a lesser extent Fe,
324 Co and Ni concentrations (Figs. 9h and 10e-h). This is confirmed by the relatively high brightness
325 of the corresponding area by HAADF-STEM (Fig. 9h). In some locations, abundant nanometer-
326 sized rods of Fe-(oxyhydr)oxides were also found among the tiny fibres of magnesium silicates
327 within the carbon gel (e.g., Fig. 9g). Overall, transition metals appear to be associated with the
328 carbon-bearing phase but selectively enriched in two domains characterized by high and low carbon
329 concentrations for the Co-rich and Mn-Fe(-Ni) enriched areas, respectively.

330 Energy-filtered STXM images and associated C-XANES spectra collected in the same areas
331 show that these chemically-heterogeneous organic carbon micro-domains display distinguishable
332 signatures (Fig. 12). Similarly to what has been found for the carbon gel embedding pol-spt in the
333 branched and elongated dissolution cavities (Fig. 6), the Mn-enriched regions display mainly
334 absorption features of carboxylic functional groups at 288.6 eV along with the presence at a lower
335 amount of aliphatic carbon at 287.7 eV (Cody et al., 1998; Benzerara et al., 2004; Bernard et al.,
336 2009). A peak at 290.4 eV was also observed. According to Chan et al. (2009), it can be indicative
337 of carboxyl groups binding iron and possibly other metals. Compared to the Mn-enriched area, the
338 Co-rich foamy region shows increased and decreased levels in aliphatics and carboxyl functional
339 groups, respectively, plus minor aromatic or olefinic carbon at 285.1 eV.

340

341 **4. Discussion and implications**

342

343 As hypothesized by Ménez et al. (2012), textural relationships provide evidence that both H-
344 adr dissolution and bastite resorption came along with the crystallization of polygonal and

345 polyhedral serpentine around the andraditic hydrogarnets and within their dissolution cavities (Figs.
346 2 and 5a-b). The pol-spt genetic link with Cr-rich hydrogarnets is also supported by EMPA showing
347 enrichment of the pol-spt in Cr and to a lesser extent in Al and Fe in comparison with the high-
348 temperatures serpentines (Fig. 3 and Supplementary Fig. 2). These elements could have been
349 inherited from both the parent H-adr and the bastite, this latter being likely the source of Mg for the
350 precipitation of pol-spt (Supplementary Fig. 2).

351 Dissolution has selectively affected the crystal cores and progressed radially toward the
352 grain rims (e.g., Figs. 5c and 7c and Supplementary Fig. 1). This process led to the formation of
353 large inner cavities interpreted by Ménez et al. (2012) as the result of a cryptoendolithic microbial
354 activity. Note that the origin of the organics found in these rocks is not discussed in the present
355 paper and readers are referred to Ménez et al. (2012) and Pasini et al. (2013) and to the extensive
356 discussions on organics' systematics that can be found within. Dissolution cavities provided the
357 open space required for polyhedral serpentine to form (Andreani et al., 2008), along with the
358 appropriate temperature conditions. Indeed, while the mesh serpentine, the bastite, and the
359 serpentine contouring spinels are representative of the static replacement of the high temperature
360 paragenesis during the first stages of serpentinization ($> 200^{\circ}\text{C}$; Klein et al., 2014), the pol-spt are
361 instead representative of crystallization occurring after complete hydration of the host pyroxene.
362 Moreover, as discussed by Ménez et al. (2012), their precipitation after H-adr, which forms below
363 200°C (Frost and Beard, 2007; Plümper et al., 2014) attests for low-temperature conditions in
364 agreement with Andreani et al. (2008). These authors also suggest a general enrichment in trivalent
365 cations as a stabilizing factor for pol-spt nucleation. This requirement is met here when considering
366 the aluminum and chromium concentrations in pol-spt, as measured by EMPA (Supplementary Fig.
367 2 and Supplementary Table 1). For iron, while pol-spt display with the vein spt the highest
368 concentrations, we did not succeed in determining the ferric iron content of pol-spt based on EMPA
369 (Pasini, 2013). Nonetheless, as H-adr iron is solely in the form of Fe(III), it may suggest that at least
370 a fraction of the pol-spt iron is present as Fe(III).

371 In our study, we observe that polyhedral and polygonal serpentines crystallized together in

372 spatially-restricted areas, hence suggesting that they likely derive from the same process. Polygonal
373 serpentine has been viewed by some authors as a more stable phase compared to chrysotile, or
374 alternatively, as an analogous of the polyhedral serpentine (Cressey et al., 2008, 2010).

375 Accordingly, polygonal and polyhedral serpentines may both form from a similar precursor through
376 different growth mechanisms. Based on textural and microstructural criteria, Andreani et al. (2008)
377 suggest that polyhedral serpentines, which are always the last serpentine type to crystallize, directly
378 nucleate and grow radially with a layer-by-layer mechanism from a proto-serpentine colloidal phase
379 containing a continuous solid skeleton of polymers or aggregates bathed in a liquid phase. Whether
380 the proto-serpentine gel includes organic carbon compounds either of biogenic or abiotic origin has
381 up to now never been documented. In the present study, the strict association of pol-spt serpentines
382 with a Mg- and Si-bearing organic phase embedding all spheroid and tubular structures and coating
383 the hydrogarnets walls (Figs. 5-7) suggests that organic carbon plays a role in the formation and
384 stabilization of polyhedral serpentine and may constitute a key component of this proto-serpentine
385 phase described by Andreani et al. (2008) as mediating the formation of polyhedral serpentines.
386 This is supported by the presence of Mg-rich C-inclusions hosted in well-crystallized serpentine in
387 the vicinity of the carbon gel (Figs. 9b and e) suggesting that organic carbon was involved in the
388 last serpentinization events affecting the rock and not lately added to the system.

389 Further investigations are nonetheless needed to confirm the systematic presence of organic
390 carbon associated with the formation of polyhedral serpentine in various settings. If true, polyhedral
391 serpentines as a common mineral of the serpentinized oceanic lithosphere (e.g., Andreani et al.,
392 2007; Baronnet et al., 2007; Rouméjon et al., 2015) may then be used as a proxy for the presence of
393 organic carbon within serpentinites. The presence of cronstedtite-derived polyhedral serpentine
394 reported in carbonaceous chondrites (Zega et al., 2006) may also support this idea. Carbonaceous
395 chondrites are known to contain a rich mixture of complex organic compounds (e.g., Schmitt-
396 Kopplin et al., 2010). As shown by Elmaleh et al. (2015), the complex oxidation mechanisms of Fe-
397 rich serpentines close to the cronstedtite endmember, which are abundant alteration products in
398 chondrites, promote molecular hydrogen production and hence potential pathways for inorganic

399 carbon reduction. If organic carbon is mandatory for pol-spt to form, then it would provide
400 constrains on the timing of abiotic organic synthesis during the aqueous alteration of carbonaceous
401 chondrites, the polyhedral serpentine being already considered as the endmember of an intense
402 alteration sequence which may have occurred early in the chondrite or parent body history
403 (Browning et al., 1996; Zega et al., 2006).

404 From another perspective, understanding how to promote the formation of pol-spt may have
405 additional implications, notably for subsurface CO₂ storage. Due to the chemical potential of
406 serpentinization to favor carbonation (i.e., CO₂ conversion into solid carbonates), ultramafic rocks
407 have long been proposed as potential hosts for long lasting and safe storage of anthropogenic CO₂
408 in the attempt to stem the currently observed consequences on climate change and ocean
409 acidification (e.g., Matter and Kelemen, 2009). One of the major criticisms raised against such a
410 technology is the high clogging potential of lizardite which subsequently forms in veins and
411 fractures following fluid-rock interactions and is commonly found as extremely fine-grained scales
412 and massive aggregates (e.g., Farough et al., 2016). If organics, by controlling the size and shape of
413 low-temperature serpentine types, promote instead the formation of pol-spt spheroids or tiny tubules
414 in veins and fractures, as observed in Figs. 2g-h, fluid flow would then be improved together with
415 the hydrodynamic properties of serpentinite.

416 Although the scattering of the data is large due to the small size of the spheroids and rods
417 compared to the electron beam size, EPMA suggest that pol-spt have incorporated a limited amount
418 of divalent metals in their structure (Fig. 3, Supplementary Fig. 2 and Supplementary Table 1).
419 Indeed, pol-spt display low concentrations in cobalt and manganese while nickel reaches higher
420 concentrations (Supplementary Fig. 2 and Supplementary Table 1). Then, instead of being
421 mobilized by aqueous fluids during hydrothermal alteration, as generally acknowledged during
422 serpentinization (Pinto et al., 20017), metals unaccommodated by the pol-spt are found in the
423 surrounding carbon gel where their speciation and mobility are apparently dictated by the
424 concentration and the type of associated organic compounds (Fig. 12). The latter can be variable at
425 the microscale, as attested by the chemically-heterogeneous organic carbon micro-domains

426 highlighted by STEM-EDXS (Figs. 9 and 11) and STXM (Fig. 12). Cobalt is systematically
427 associated with carbon, sometimes in the form of well-crystallized Co-oxides accompanied by
428 lower concentrations of Mn, Ni, and Fe (Figs. 9e-h, 10a-b and 11). Mn-oxides are found in carbon-
429 poor areas also enriched in Fe and Ni, forming nanometric crusts around pol-spt spheroids (Figs. 9h,
430 10c-h and 11).

431 Different processes can account for the local formation of these metallic oxides. Both Co
432 and Mn in their divalent form are soluble ions in hydrothermal fluids and the presence of metallic
433 oxides strongly suggests that oxidation, at least partial, occurred, turning Co(II) and Mn(II) into
434 insoluble Co(III) and Mn(III) or Mn(IV), and leading to the precipitation of Co- and Mn-oxides.
435 Whereas in the open ocean, organic-metal complexation reduces metal reactivity, increases their
436 solubility and limits their scavenging into or onto particulate phases (Bennett et al., 2008), the
437 presence of organic compounds in the present system did not play the same protective role as
438 oxidation could have been responsible for the immobilization of metals. Although oxidative
439 dissolution, as observed in the case of hydrothermal sulfides (German et al., 1991), cannot be totally
440 excluded, Co and Mn oxidation is a process primarily known to be mediated by bacteria (Murray et
441 al., 2007), in agreement with Ménez et al. (2012) who hypothesized that biological activity could
442 have been responsible for H-dr dissolution. Mn(II) oxidation can occur by direct enzymatic
443 activity (e.g., Tebo et al., 2004) or by exposure to reactive oxygen species produced by cells
444 (Learman et al., 2011). Mn(II) biological oxidation was demonstrated to represent an important
445 process in the formation of ferromanganese nodules and crusts (Nealson, 2006), sometimes also
446 enriched in Co(III) (Lee and Tebo, 1994). In aquatic environments, microbial Co and Mn oxidation
447 were also shown to be linked but the oxidation of Co can also possibly be related to the high
448 oxidative capabilities of poorly-crystalline Mn-oxides (Liao et al. 2011; Murray et al., 2007). These
449 latter are indeed known to strongly control the transfer of metals in polluted systems (Borch et al.,
450 2010; Tebo et al., 2004). Due to their high sorptive capacities, Mn-oxides can also adsorb or
451 incorporate substantial amount of metals such as Co, Ni and Fe (Nealson, 2006), as observed here
452 (Figs 10 and 11). Accordingly, in our samples, they likely contributed to the enrichment in metals

453 of the organic C-bearing phases.

454 The local enrichments in transition metals and the nucleation of nanocrystallites may also
455 have been driven differentially by the organic matrix itself, depending on the affinity of metals with
456 the reactive organic functional groups locally present. Based on what was postulated by Ménez et
457 al. (2012), the organic compounds found in these rocks may have derived from the presence of
458 former cryptoendolithic microbial ecosystems solubilizing substrates by structuring themselves in
459 the form of biofilm. Biofilm are described as gel-like structures composed of cells and EPS showing
460 high reactive site densities (Ha et al., 2010). Metallic divalent cations, leached from H-adr, bastite
461 and inherited Fe-ox, may then have been differentially trapped by the negatively-charged functional
462 groups present in EPS. By imposing diffusion-limited processes, low permeability EPS, well
463 acknowledged to strongly impact metal dynamics (e.g., Templeton et al., 2001; Wang et al., 2016;
464 Warren and Haack, 2001), may also have contributed to accumulate Co and Mn in spatially-
465 restricted areas, hence leading to the precipitation of metallic oxides once the supersaturation with
466 respect to these oxides was locally reached. STXM imaging highlights that local enrichments in
467 transition metals are selectively associated with different types and concentrations of organic carbon
468 (Fig. 12). Cobalt was found within a carbon-rich gel-like mixture containing higher amount of
469 aliphatics and lower amount of carboxylic compounds in comparison with the Mn-enriched C-poor
470 micro-domain. However, the higher abundance of carboxyl groups in the Mn-enriched area suggests
471 that, in this micro-domain, organic compounds may have been oxidized by the Mn-oxides, hence
472 exerting locally a control on the redox state of the system. Note in addition that Co-oxides are
473 known catalysts for abiotic organic synthesis down to 30°C (e.g., Melaet et al., 2014; Varma et al.,
474 2018). In this respect, once accumulated in the organic matrix, they also likely impacted the
475 evolution of these organic molecules. However, the STXM spectrum of the Mn/Fe-bearing felt
476 presents similarities with the one obtained in the carbon gel embedding pol-spt in the H-adr cavities
477 (Fig. 6) and for which no enrichment in transition metals was shown. It will hence deserve further
478 investigations notably on metal speciation.

479 Overall, whatever the detailed mechanisms involved, our observations demonstrate that

480 organic compounds have the potential to immobilize metals in the form of metallic oxides or as
481 metal ions adsorbed onto organic matrices during low-temperature hydrothermal alteration of the
482 mantle-derived crust. If the impact of such processes on metal cycles is difficult to assess at the
483 scale of the oceanic lithosphere in the present state of knowledge, it may have implications for
484 ophiolites where active serpentinization also occurs. Ophiolitic massifs experiencing supergene
485 alteration are the target for ore exploration and mining. Notably, tropical alteration of ophiolites
486 yields lateritic cap rocks locally enriched in Co and Mn (Butt and Cluzel, 2013). As an illustration,
487 Dublet et al. (2017) recently described the vertical changes in Co and Mn speciation along a lateritic
488 regolith developed as a function of weathering stage upon peridotites from New Caledonia where
489 mining activities exploit nickel-bearing ore over 6 000 km². They raised the question of the role of
490 Mn- vs. Fe-(oxyhydr)oxides on Co speciation and on the long-term stabilization of metals at the
491 whole regolith scale. Considering that the ophiolitic massif might host active microbial
492 communities over a large depth, as it was recently demonstrated in Oman (Miller et al., 2016;
493 Rempfert et al. 2017), we suggest that organic compounds along with microbial activities should
494 also be investigated in the regolith and its underlying basement to assess their respective impact on
495 Mn and Co speciation (\pm Ni and Fe) and hence on supergene ore formation, as already highlighted
496 for gold or platinum-group elements (Reith et al., 2010, 2016).

497

498 **5. Conclusions**

499

500 We show in this study that high resolution spectroscopy and microscopy are a powerful
501 approach to image organic compounds trapped in the porosity of serpentinites and to investigate
502 their co-occurrences with metals and minerals. We strongly suggest that organic compounds, whose
503 origin can be diverse in serpentinites (both abiotic and biogenic), locally influence low temperature
504 (< 200°C) fluid-rock interactions in the serpentinizing oceanic lithosphere with consequences on
505 metal distribution, speciation and hence mobility, as well as on the nature and structure of late stage
506 mineralizations such as polygonal and polyhedral serpentines. Given the growing body of evidences

507 showing that the serpentinized oceanic lithosphere constitutes a large habitat for life and that
508 serpentinization reactions have a high potential for abiotic organic synthesis, it is then reasonable to
509 expect such processes to be widespread in ultramafic rocks.

510

511 **Acknowledgements**

512

513 The authors are grateful to A. Cipriani (Univ. Modena e Reggio Emilia) who made available the
514 sample collection recovered during the S22 expedition. We thank A. Gualtieri for his TEM
515 expertise on serpentine, O. Boudouma for the assistance during SEM, D. Troadec for milling the
516 FIB ultrathin section, and Javier Escartin for the bathymetric map of the Sierra Leone Fracture
517 Zone. B.M. thanks Alexandre Gélabert and Thaïs Couasnon for stimulating discussion along with
518 Jeff Alt and one other anonymous reviewer for constructive reviews. This work was supported by
519 the French National Research Agency ANR through the deepOASES project granted to B.M. [grant
520 number ANR-14-CE01-0008], Fondazione Cassa di Risparmio di Modena through the
521 CARBRIDGE project (granted to D.B.), and an ECORD Research Grant 2010 to V.P. Support of
522 the Deep Energy Community from the Deep Carbon Observatory awarded by Alfred P. Sloan
523 Foundation is also acknowledged. STXM data were acquired at ALS beamline 5.3.2.2, which is
524 supported by the Director of the Office of Science, Department of Energy [contract number DE-
525 AC02-05CH11231]. Special thanks go to D. Kilcoyne for his expert support. The TEM facility at
526 IMPMC was purchased owing to a support by Region Ile-de-France grant SESAME 2000 E 1435.
527 This is IGP contribution n° XXXXX.

528

529 **References**

- 530 Andreani, M., Mével, C., Boullier, A.M., Escartín, J., 2007. Dynamic control on serpentine
531 crystallization in veins: constraints on hydration processes in oceanic peridotites.
532 *Geochemistry Geophysics Geosystems* 8, Q02012.
- 533 Andreani, M., Grauby, O., Baronnet, A., Munoz, M., 2008. Occurrence, composition and growth of

534 polyhedral serpentine. *European Journal of Mineralogy* 20, 159-171.

535 Baronnet, A., Devouard, B., 1996. Topology and crystal growth of natural chrysotile and polygonal
536 serpentine. *Journal of Crystal Growth* 166, 952-960.

537 Baronnet, A., Devouard, B., 2005. Microstructures of common polygonal serpentines from axial
538 HRTEM imaging, electron diffraction, and lattice simulation data. *The Canadian Mineralogist*
539 43, 513-542.

540 Baronnet, A., Andreani, M., Grauby, O., Devouard, B., Nitsche, S., Chaudanson, D., 2007. Onion
541 morphology and microstructure of polyhedral serpentine. *American Mineralogist* 92, 687-690.

542 Bassim, B.T., Kilcoyne, A.L.D., Scott, K., Chou, T., Wirick, S., Cody, G., Stroud, R.M., 2012.
543 Minimizing damage during FIB sample preparation of soft materials. *Journal of Microscopy*
544 245, 288-301.

545 Bennett, S.A., Achterberg, E.P., Connelly, D.P., Statharn, P.J., Fones, G.R., Gernian, C.R., 2008.
546 The distribution and stabilisation of dissolved Fe in deep-sea hydrothermal plumes. *Earth and*
547 *Planetary Science Letters* 270, 157-167.

548 Bennett, S.A., Statham, P.J., Green, D.R.H., Le Bris, N., McDermott, J.M., Prado, F., Rouxel, O.J.,
549 Von Damm, K., German, C.R., 2011. Dissolved and particulate organic carbon in
550 hydrothermal plumes from the East Pacific Rise, 9°50'N. *Deep Sea Research Part I* 58, 922-
551 931.

552 Benzerara, K., Yoon, T.H., Tyliczszak, T., Constantz, B., Spormann, A.M., Brown Jr., G.E., 2004.
553 Scanning transmission X-ray microscopy study of microbial calcification. *Geobiology* 2, 249-
554 259.

555 Benzerara, K., Menguy, N., Guyot, F., Vanni, C., Gillet, P., 2005. High resolution study of silicate-
556 carbonate-micro-organism interface prepared by focused ion beam (FIB). *Geochimica et*
557 *Cosmochimica Acta* 69, 1413-1422.

558 Bernard, S., Benzerara, K., Beyssac, O., Brown Jr., G.E., Stamm, L.G., Durringer, P., 2009.
559 Ultrastructural and chemical study of modern and fossil sporoderms by Scanning
560 Transmission X-ray Microscopy (STXM). *Review of Palaeobotany and Palynology* 156, 248-

561 261.

562 Borch, T., Kretzschmar, R., Kappler, A., Van Cappellen, P., Ginder-Vogel, M., Voegelin, A.,
563 Campbell, K., 2010. Biogeochemical redox processes and their impact on contaminant
564 dynamics. *Environmental Science & Technology* 44, 15-23.

565 Boyd, P.W., Ellwood, M.J., 2010. The biogeochemical cycle of iron in the ocean. *Nature*
566 *Geoscience* 3, 675-682.

567 Browning, L.B., McSween, H.Y. Jr., Zolensky, M.E., 1996. Correlated alteration effects in CM
568 carbonaceous chondrites. *Geochimica et Cosmochimica Acta* 60, 2621-2633.

569 Butt, C.R., Cluzel, D., 2013. Nickel laterite ore deposits: weathered serpentinite. *Elements* 9, 123-
570 128.

571 Chan, C.S., Fakra, S.C., Edwards, D.C., Emerson, D., Banfield, J.F., 2009. Iron oxyhydroxide
572 mineralization on microbial extracellular polysaccharides. *Geochimica et Cosmochimica Acta*
573 73, 3807-3818.

574 Cody, G.D., Ade, H., Wirick, S., Mitchell, G.D., Davis, A., 1998. Determination of chemical-
575 structural changes in vitrinite accompanying luminescence alteration using C-NEXAFS
576 analysis. *Organic Geochemistry* 28, 441-455.

577 Cressey, G., Cressey, B.A., Wicks, F.J., 2008. Polyhedral serpentine: a spherical analogue of
578 polygonal serpentine? *Mineralogical Magazine* 72, 1229-1242.

579 Cressey, G., Cressey, B.A., Wicks, F.J., Yada, K., 2010. A disc with fivefold symmetry: the
580 proposed fundamental seed structure for the formation of chrysotile asbestos fibres, polygonal
581 serpentine fibres and polyhedral lizardite spheres. *Mineralogical Magazine* 74, 29-37.

582 Dublet, G., Juillot, F., Brest, J., Noël, V., Fritsch, E., Proux, O., Olivi, L., Ploquin, F., Morin, G.,
583 2017. Vertical changes of the Co and Mn speciation along a lateritic regolith developed on
584 peridotites (New Caledonia). *Geochimica et Cosmochimica Acta* 217, 1-15.

585 Elmaleh, A., Bourdelle, F., Caste, F., Benzerara, K., Leroux, H., Devouard, B., 2015. Formation
586 and transformations of Fe-rich serpentines by aqueous alteration in asteroids: a nanoscale
587 study of the Murray chondrite. *Geochimica et Cosmochimica Acta* 158, 162-178.

588 Farough, A., Moore, D.E., Lockner, D.A., Lowell, R.P., 2016. Evolution of fracture permeability of
589 ultramafic rocks undergoing serpentinization at hydrothermal conditions: An experimental
590 study. *Geochemistry, Geophysics, Geosystems* 17, 44-55.

591 Field, M.P., Sherrell, R.M., 2000. Dissolved and particulate Fe in a hydrothermal plume at 9°45'N,
592 East Pacific Rise: Slow Fe(II) oxidation kinetics in Pacific plumes. *Geochimica et*
593 *Cosmochimica Acta* 64, 619-628.

594 Fitzsimmons, J.N., John, S.G., Marsay, C.M., Hoffman, C.L., Nicholas, S.L., Toner, B.M., German,
595 C.R., Sherrell, R.M., 2017. Iron persistence in a distal hydrothermal plume supported by
596 dissolved–particulate exchange. *Nature Geoscience* 10, 195-201.

597 Frost, B.R., Beard, J.S., 2007. On silica activity and serpentinization. *Journal of Petrology* 48,
598 1351–1368.

599 German, C.R., Campbell, A.C., Edmond, J.M., 1991. Hydrothermal scavenging at the Mid-Atlantic
600 Ridge: modification of trace element dissolved fluxes. *Earth and Planetary Science Letters*
601 107, 101-114.

602 Ha, J., Gélabert, A., Spormann, A.M., Brown, G.E., Jr., 2010. Role of extracellular polymeric
603 substances in metal ion complexation on *Shewanella oneidensis*: Batch uptake,
604 thermodynamic modeling, ATR-FTIR, and EXAFS study. *Geochimica et Cosmochimica Acta*
605 74, 1-15.

606 Hawkes, J.A., Connelly, D.P., Gledhill, M., Achterberg, E.P., 2013. The stabilization and
607 transportation of dissolved iron from high temperature hydrothermal vent systems. *Earth and*
608 *Planetary Science Letters* 375, 280-290.

609 Hawkes, J.A., Rossel, P.E., Stubbins, A., Butterfield, D., Connelly, D.P., Achterberg, E.P.,
610 Koschinsky, A., Chavagnac, V., Hansen, C.T., Bach, W., Dittmar, T., 2015. Efficient removal
611 of recalcitrant deep-ocean dissolved organic matter during hydrothermal circulation. *Nature*
612 *Geoscience* 8, 856-860.

613 Kawka, O.E., Simoneit, B.R.T., 1987. Survey of hydrothermally-generated petroleums from the
614 Guaymas Basin spreading center. *Organic Geochemistry* 11, 311-328.

615 Klein, F., Bach, W., Humphris, S.E., Kahl, W.-A., Jöns, N., Moskowitz, B., Berquó, T.S., 2014.
616 Magnetite in seafloor serpentinite-Some like it hot. *Geology* 42, 135-138.

617 Klevenz, V., Bach, W., Schmidt, K., Hentscher, M., Koschinsky, A., Petersen, S., 2011.
618 Geochemistry of vent fluid particles formed during initial hydrothermal fluid-seawater mixing
619 along the Mid-Atlantic Ridge. *Geochemistry, Geophysics Geosystems* 12 (10), Q0AE05.

620 Kilcoyne, A.L., Tyliszczak, T., Steele, W.F., Fakra, S., Hitchcock, P., Franck, K., Anderson, E.,
621 Harteneck, B., Rightor, E.G., Mitchell, G.E., Hitchcock, A.P., Yang, L., Warwick, T., Ade,
622 H., 2003. Interferometer-controlled scanning transmission X-ray microscopes at the
623 Advanced Light Source. *Journal of Synchrotron Radiation* 10, 125–136.

624 Konn, C., Charlou, J.L., Holm, N.G., Mousis, O., 2015. The production of methane, hydrogen, and
625 organic compounds in ultramafic-hosted hydrothermal vents of the Mid-Atlantic Ridge.
626 *Astrobiology* 15, 381-399.

627 Lang, S.Q., Butterfield, D.A., Lilley, M.D., Paul Johnson, H., Hedges, J.I., 2006. Dissolved organic
628 carbon in ridge-axis and ridge-flank hydrothermal systems. *Geochimica et Cosmochimica*
629 *Acta* 70, 3830-3842.

630 Lau, B.L.T., Hsu-Kim H., 2008. Precipitation and growth of zinc sulfide nanoparticles in the
631 presence of thiol-containing natural organic ligands. *Environmental Science & Technology*
632 42, 7236-7241.

633 Learman, D.R., Wankel, S.D., Webb, S.M., Martinez, N., Madden, A.S., Hansel, C.M., 2011.
634 Coupled biotic-abiotic Mn(II) oxidation pathway mediates the formation and structural
635 evolution of biogenic Mn oxides. *Geochimica et Cosmochimica Acta* 75, 6048-6063.

636 Lee, Y., Tebo, B.M., 1994. Cobalt(II) oxidation by the marine manganese(II)-oxidizing *Bacillus* sp.
637 strain SG-1. *Applied and Environmental Microbiology* 60, 2949-2957.

638 Lepot, K., Benzerara, K., Brown, G.E., Jr., Philippot P., 2009. Organic matter heterogeneity in 2.72
639 Ga stromatolites: alteration versus preservation by sulphur incorporation. *Geochimica et*
640 *Cosmochimica Acta* 73, 6579-6599.

641 Liao, L., Xu, X.W., Jiang, X.W., Wang, C.S., Zhang, D.S., Ni, J.Y., Wu, M., 2011. Microbial

642 diversity in deep-sea sediment from the cobalt-rich crust deposit region in the Pacific Ocean.
643 FEMS Microbiology Ecology 78, 565-585.

644 Mason, O.U., Nakagawa, T., Rosner, M., Van Nostrand, J.D., Zhou, J., Maruyama, A., Fisk, M.R.,
645 Giovannoni, S.J., 2010. First investigation of the microbiology of the deepest layer of ocean
646 crust. PLoS One 5:e15399.

647 Matter, J.M., Kelemen, P.B., 2009. Permanent storage of carbon dioxide in geological reservoirs by
648 mineral carbonation. Nature Geoscience 2, 837-841.

649 Melaet, G., Ralston, W.T., Li, C.S., Alayoglu, S., An, K., Musselwhite, N., Kalkan, B., Somorjai,
650 G.A., 2014. Evidence of highly active cobalt oxide catalyst for the Fischer-Tropsch synthesis
651 and CO₂ hydrogenation. Journal of the American Chemical Society 136, 2260-2263.

652 Ménez, B., Pasini, V., Brunelli, D., 2012. Life in the hydrated suboceanic mantle. Nature
653 Geoscience 5, 133-137.

654 Miller, H.M., Matter, J.M., Kelemen, P., Ellison, E.T., Conrad, M.E., Fierer, N., Ruchala, T.,
655 Tominaga, M., Templeton, A.S., 2016. Modern water/rock reactions in Oman hyperalkaline
656 peridotite aquifers and implications for microbial habitability. Geochimica et Cosmochimica
657 Acta 179, 217-241.

658 Monnin, C., Chavagnac, V., Boulart, C., Ménez, B., Gérard, M., Gérard, E., Pisapia, C.,
659 Quéméneur, M., Erauso, G., Postec, A., Guentas-Dombrowski, L., Payri, C., Pelletier, B.,
660 2014. Fluid chemistry of the low temperature hyperalkaline hydrothermal system of Prony
661 Bay (New Caledonia). Biogeosciences 11, 5697-5706.

662 Mottl, M.J., McConachy, T.F., 1990. Chemical processes in buoyant hydrothermal plumes on the
663 East Pacific Rise near 21-degrees-N. Geochimica et Cosmochimica Acta 54, 1911-1927.

664 Murray, K.J., Webb, S.M., Bargar, J.R., Tebo, B.M., 2007. Indirect oxidation of Co(II) in the
665 presence of the marine Mn(II)-oxidizing bacterium *Bacillus* sp strain SG-1. Applied and
666 Environmental Microbiology 73, 6905-6909.

667 Nealson, K.H., 2006. The manganese-oxidizing bacteria. In: Prokaryotes (Dworkin, M., Falkow, S.,
668 Rosenberg, E., Schleifer, K.H., Stackebrandt, E., eds), Springer, New York, N.Y., vol. 5, 222-

669 231.

670 Pasini, V., 2013. Biopetrology of the hydrating mantle along Mid-Ocean ridges. Ph.D manuscript.
671 Università di Modena e Reggio Emilia & Institut de Physique du Globe de Paris, 308 p.

672 Pasini, V., Brunelli, D., Dumas, P., Sandt, C., Frederick, J., Benzerara, K., Bernard, S., Ménez, B.,
673 2013. Low temperature hydrothermal oil and associated biological precursors in serpentinites
674 from Mid-Ocean ridge. *Lithos* 178, 84-95.

675 Pinto, V.H.G., Manatschal, G., Karpoff, A.M., Ulrich, M., Viana, A.R., 2017. Seawater storage and
676 element transfer associated with mantle serpentinization in magma-poor rifted margins: A
677 quantitative approach. *Earth and Planetary Science Letters* 459, 227-237.

678 Plümper, O., Beinlich, A., Bach, W., Janots, E., Austrheim, H., 2014. Garnets within geode-like
679 serpentinite veins: Implications for element transport, hydrogen production and life-
680 supporting environment formation. *Geochimica et Cosmochimica Acta* 141, 454-471.

681 Peive, A.A., Savel'eva, G.N., Skolotnev, S.G., Simonov, V.A., 2003. Tectonics and origin of the
682 oceanic crust in the region of 'dry' spreading in the Central Atlantic (7°10'5"N). *Geotectonics*
683 37, 3-25.

684 Reith, F., Fairbrother, L., Nolze, G., Wilhelmi, O., Clode, P.L., Gregg, A., Parsons, J.E., Wakelin,
685 S.A., Pring, A., Hough, R., Southam, G., Brugger, J., 2010. Nanoparticle factories: biofilms
686 hold the key to gold dispersion and nugget formation. *Geology* 38, 843-846.

687 Reith, F., Zammit, C.M., Saad Shar, S., Etschmann, B., Bottrill, R., Southam, G., Ta, C., Kilburn,
688 M., Oberthür, T., Ball, A.S., Brugger, J., 2016. Biological role in the transformation of
689 platinum-group mineral grains. *Nature Geoscience* 9, 294-298.

690 Rempfert, K.R., Miller, H.M., Bompard, N., Nothaft, D., Matter, J.M., Kelemen, P., Fierer, N.,
691 Templeton, A.S., 2017. Geological and geochemical controls on subsurface microbial life in
692 the Samail ophiolite, Oman. *Frontiers in Microbiology* 8, 56.

693 Resing, J.A., Sedwick, P.N., German, C.R., Jenkins, W.J., Moffett, J.W., Sohst, B.M., Tagliabue,
694 A., 2015. Basin-scale transport of hydrothermal dissolved metals across the South Pacific
695 ocean. *Nature* 523, 200-203.

696 Rossel, P.E., Stubbins, A., Rebling, T., Koschinsky, A., Hawkes, J.A., Dittmar, T., 2017. Thermally
697 altered marine dissolved organic matter in hydrothermal fluids. *Organic Geochemistry* 110,
698 73-86.

699 Rouméjon, S., Cannat, M., Agrinier, P., Godard, M., Andreani, M., 2015. Serpentinization and fluid
700 pathways in tectonically exhumed peridotites from the southwest Indian ridge (62-65°E).
701 *Journal of Petrology* 56, 703-734.

702 Sander, S.G., Koschinsky, A., 2011. Metal flux from hydrothermal vents increased by organic
703 complexation. *Nature Geoscience* 4, 145-150.

704 Sander, S.G., Koschinsky, A., Massoth, G., Stott, M., Hunter, K.A., 2007. Organic complexation of
705 copper in deep-sea hydrothermal vent systems. *Environmental Chemistry* 4, 81-89.

706 Sands, C.M., Connelly, D.P., Statham, P.J., German, C.R., 2012. Size fractionation of trace metals
707 in the Edmond hydrothermal plume, Central Indian Ocean. *Earth and Planetary Science*
708 *Letters* 319-320, 15-22.

709 Santelli, C.M., Orcutt, B.N., Banning, E., Bach, W., Moyer, C.L., Sogin, M.L., Staudigel, H.,
710 Edwards, K.J., 2008 Abundance and diversity of microbial life in ocean crust. *Nature* 453,
711 653-656.

712 Schmitt-Kopplin, P., Gabelica, Z., Gougeon, R.D., Fekete, A., Kanawati, B., Harir, M., Gebefuegi,
713 I., Eckel, G., Hertkorn, N., 2010. High molecular diversity of extraterrestrial organic matter in
714 Murchison meteorite revealed 40 years after its fall. *Proceedings of the National Academy of*
715 *Sciences of the United States of America* 107, 2763-2768.

716 Schneider, C.A., Rasband, W.S., Eliceiri, K.W., 2012. NIH Image to ImageJ: 25 years of image
717 analysis. *Nature Methods* 9, 671-675.

718 Schrenk, M.O., Brazelton, W.J., Lang, S.Q., 2013. Serpentinization, carbon and deep life. In:
719 Hazen, R.M., Jones, A.P., Baross, J.A. (Eds.), *Carbon in Earth. Reviews in Mineralogy and*
720 *Geochemistry*, 75. Mineralogical Society of America, Geochemical Society, pp. 575-606.

721 Seyfried, W.E., Jr., Pester, N.J., Tutolo, B.M., Ding, K., 2015. The Lost City hydrothermal system:
722 Constraints imposed by vent fluid chemistry and reaction path models on seafloor heat and

723 mass transfer processes. *Geochimica et Cosmochimica Acta* 163, 59-79.

724 Sharkov, E., 2012. Cyclic development of axial parts of slow-spreading ridges: Evidence from
725 Sierra Leone area, the Mid-Atlantic Ridge, 5-7°N. In: Sharkov, E. (Ed.), *Tectonics - Recent*
726 *Advances*, pp. 3-36.

727 Simoneit, B.R.T., Lein, A.Y., Peresyphkin, V.I., Osipov, G.A., 2004. Composition and origin of
728 hydrothermal petroleum and associated lipids in the sulfide deposits of the Rainbow Field
729 (Mid-Atlantic Ridge at 36°N). *Geochimica et Cosmochimica Acta* 68, 2275-2294.

730 Statham, P.J., German, C.R., Connelly, D.P., 2005. Iron(II) distribution and oxidation kinetics in
731 hydrothermal plumes at the Kairei and Edmond vent sites, Indian Ocean. *Earth and Planetary*
732 *Science Letters* 236, 588-596.

733 Tebo, B.M., Bargar, J.R., Clement, B.G., Dick, G.J., Murray, K.J., Parker, D., Verity, R., Webb,
734 S.M., 2004. Biogenic manganese oxides: Properties and mechanisms of formation. *Annual*
735 *Review of Earth and Planetary Sciences* 32, 287-328.

736 Templeton, A.S., Trainor, T.P., Traina, S.J., Spormann, A.M., Brown, G.E., 2001. Pb(II)
737 distributions at biofilm-metal oxide interfaces. *Proceedings of the National Academy of*
738 *Sciences of the United States of America* 98, 11897-11902.

739 Toner, B.M., Fakra, S.C., Manganini, S.J., Santelli, C.M., Marcus, M.A., Moffett, J.W., Rouxel, O.,
740 German, C.R., Edwards, K.J., 2009. Preservation of iron(II) by carbon-rich matrices in a
741 hydrothermal plume. *Nature Geoscience* 2, 197-201.

742 Varma, S.J., Muchowska, K.B., Chatelain, P., Moran, J., 2018. Native iron reduces CO₂ to
743 intermediates and end-products of the acetyl-CoA pathway. *Nature Ecology & Evolution* 2,
744 1019-1024.

745 Warren, L.A., Haack, E.A., 2001. Biogeochemical controls on metal behaviour in freshwater
746 environments. *Earth-Science Reviews* 54, 261-320.

747 Wang, Y., Gélabert, A., Michel, F.M., Choi, Y., Gescher, J., Ona-Nguema, G., Eng, P.J., Bargar,
748 J.R., Farges, F., Spormann, A.M., Brown, G.E., Jr, 2016. Effect of biofilm coatings at metal-
749 oxide/water interfaces I: Pb(II) and Zn(II) partitioning and speciation at *Shewanella*

750 *oneidensis*/metal-oxide/water interfaces. *Geochimica et Cosmochimica Acta* 188, 368-392.

751 Wu, J., Wells, M.L., Remember, R., 2011. Dissolved iron anomaly in the deep tropical–subtropical
752 Pacific: Evidence for long-range transport of hydrothermal iron. *Geochimica et*
753 *Cosmochimica Acta* 75, 460-468.

754 Zega, T.J., Garvie, L.A.J., Dódonny, I., Friedrich, H., Stroud, R.M., Buseck, P.R., 2006. Polyhedral
755 serpentine grains in CM chondrites. *Meteoritic & Planetary Science* 41, 681-688.

756

757 **Figure captions**

758

759 **Fig. 1.** (a) bathymetric map of the 0-10° N region showing within a white rectangle the location of
760 the non-transform Sierra Leone Fracture Zone (FZ; 7°10'5 N) in the equatorial Mid-Atlantic Ridge
761 where the sample S2232-17 has been dredged (“mbsl” stands for meters below sea level). (b)
762 enlarged view of (a). (c) optical image of a cut section of the serpentinized S2232-17 rock; olivine
763 was replaced by serpentine and magnetite exhibiting a characteristic mesh texture (mesh-spt);
764 orthopyroxene was replaced by fine grained lizardite, defined as bastite (bast). Late veins of
765 serpentine crosscut the whole (spt-vein). (d) photomicrograph in transmitted plane polarized light
766 showing andraditic hydrogarnet (H-adr) ± iron oxides distributed along exsolution lamellae in the
767 bastitized orthopyroxene. Clusters of hydrogarnets were also found close to the orthopyroxenes,
768 filling veins and microfractures.

769

770 **Fig. 2.** SEM images of polygonal and polyhedral serpentine (pol-spt) rods and spherules of variable
771 sizes (10-1,000 nm) found (a) surrounding a pierced andraditic hydrogarnet (H-adr), (b) filling in
772 the interior of a fractured H-adr crystal enclosed in bastite (bast). (c) and (d) are enlarged views of a
773 hydrogarnet selvage with (d) being located in (c) with a white rectangle. (e) and (f) show that the
774 pol-spt coverage is uniform in the cavity where a hydrogarnet was formerly present. (f), which is a
775 magnified view of (e) (location indicated by a white rectangle), shows indentation of the pol-spt
776 within the fine grained orientated bastite. As hypothesized by Ménez et al. (2012), pol-spt are
777 progressively replacing hydrogarnets in this rock with (g) illustrating an advanced dissolution stage
778 with a hydrogarnet almost fully replaced by pol-spt. White arrows in (g) depict tiny veins (< 5 µm
779 in width) of pol-spt branching out from the former H-adr location (detail shown in (h)). (a), (b) and
780 (g) are reproduced from Ménez et al. (2012) with permission.

781

782 **Fig. 3.** Cr₂O₃ (wt.%) versus X_{Fe} diagram established from EMPA collected on the 5 groups of
783 serpentines identified in the rock: the serpentine after olivine in the mesh texture (mesh spt), the

784 bastite after orthopyroxene (bast), the serpentine after olivine contouring spinels (spl spt), the
785 polygonal and polyhedral serpentines associated with hydrogarnets (pol-spt) and the serpentine
786 found in the late veins crosscutting the rock (vein spt) (Fig. 1c). The uncertainties associated to
787 EMPA are within the symbol dimensions. X_{Fe} is defined as (total Fe)/(total Fe + Mg) and expresses
788 the fraction of iron incorporated into serpentine. The enrichment in Cr and to a lesser extent in Fe
789 and Al (see also Supplementary Fig. 2 and Supplementary Table 1) of the pol-spt, are in agreement
790 with formation from hydrogarnet dissolution, the hydroandradite displaying mean formula of
791 $\text{Ca}_{2.71}(\text{Fe}_{1.61}^{3+}, \text{Ti}_{0.01}, \text{Al}_{0.17}, \text{Cr}_{0.03}, \text{Mg}_{0.02})(\text{Si}_{2.92}\text{O}_{10.93})(\text{OH})_{1.07}$.

792

793 **Fig. 4.** (a) TEM image collected on a FIB ultrathin section and showing a submicrometric spheroid
794 grown in an elongated cavity inside a hydrogarnet (H-adr). The corresponding FIB section is shown
795 in Fig. 6b. The spheroid was identified by SAED as geodesic polyhedral serpentine (pol-spt) whose
796 model is drawn in the lower left inset in (b). The diffraction pattern is characteristic of a
797 polycrystalline aggregate, with spots aligned along circles of increasing diameter due to the multiple
798 orientations of each serpentine triangular facet. Measured inter-planar distances are compatible with
799 lizardite lattice, in agreement with Andreani et al. (2008) who reported on the strict short-range
800 similarity of the structure of polyhedral serpentine and lizardite, based on Raman spectroscopic
801 characteristics.

802

803 **Fig. 5.** The nucleation and growth of polyhedral and polygonal serpentine (pol-spt) from the
804 hydrogarnet (H-adr) dissolution appear to be mediated by a carbon-bearing gel-like phase. (a) SEM
805 image of a H-adr cavity milled by FIB revealing enclosed pol-spt of variable size growing on a
806 granular H-adr surface (see Supplementary Fig. 1 for SEM views of the corresponding H-adr and
807 FIB foil). (b) TEM image detailing the pol-spt/H-adr interface. Submicrometric chrysotile fibres are
808 also visible. The close connection between pol-spt and H-adr, highlighted at the location shown by
809 the white asterisk, again suggests that pol-spt grew at the expense of hydrogarnets, hence
810 confirming the genetic link between both. Moreover, it highlights continuous coating of the

811 assemblage by a gel-like phase (depicted by black arrows). The corresponding FIB section is shown
812 in Fig. 7c. (c) magnified SEM view of H-adr dissolution cavities in which carbon veils can be
813 found. (d) TEM image showing a 15 sector (upper fibre) and a 30 sector (bottom fibre) polygonal
814 serpentine wet by a jelly film of carbon interfacing between the serpentine and the H-adr walls. The
815 corresponding FIB section is shown in Fig. 6b. Star and diamond correspond to the locations of the
816 EDXS spectra shown in (e) and collected on the carbon gel and the pol-spt, respectively. (e)
817 associated EDXS spectra showing that the carbon gel is also bearing Si, Mg, and to a lesser extent,
818 Ca and Fe, likely inherited from the hydrogarnet and the bastite. (f) HAADF-STEM image of a
819 serpentine spheroid confirming the carbon gel to also bear heavier elements in addition to carbon.
820 (g) associated STEM-EDXS elemental image showing the distribution of carbon (green).

821

822 **Fig. 6.** STXM characterization at the C K-edge of the carbon gel associated with polyhedral rods
823 and polygonal serpentine spheroids (pol-spt) occurring in dissolution cavities of hydrogarnet (H-
824 adr). (a) SEM image of a subhedral andraditic hydrogarnet showing pol-spt spreading. The location
825 where the foil was milled is indicated by the orange dashed line. (b) SEM image of the FIB foil
826 where dissolution pits and cavities filled with pol-spt spheroids are visible along with pol-spt
827 covering the H-adr rim. The platinum coating aimed at protecting milled volumes before
828 excavation. (c) TEM enlarged view of the area shown by a white square in (b) where pol-spt have
829 crystallized in the H-adr dissolution cavity. White asterisk corresponds to the location of the pol-spt
830 geodesic spheroid shown in Fig. 4. (d) composite STXM map showing the distribution of organic
831 carbon (in red) in the mineral matrix (in green). The STXM image is located using a black square in
832 (b). It confirms the organic nature of the carbon gel. (e) associated C-XANES spectrum showing
833 mainly X-ray absorption of carboxyl functional groups at 288.6 eV.

834

835 **Fig. 7.** (a) SEM image in false colors of a mélange of polyhedral and polygonal serpentines (pol-spt
836 in green), along with aggregated nanometric fibres forming a felt wet by a carbon-bearing matrix
837 (yellow), all filling the cracks and voids of an andraditic hydrogarnet (H-adr in blue) hosting Fe-

838 oxides (orange). (b) SEM image of a H-adr where the FIB foil displayed in (c) was milled along the
839 orange dashed line. It shows dissolution pits piercing its surface. SEM image of the FIB foil in (c)
840 shows that these pits relate to deep inner and various-sized dissolution cavities enclosing large
841 quantity of felt in H-adr. (d) associated TEM image showing pol-spt enclosed in aggregated tiny
842 fibres likely responsible for the felt texture.

843

844 **Fig. 8.** (a) SEM image of a large accumulation of carbon-bearing felt embedding numerous
845 polyhedral and polygonal serpentines (pol-spt) and trapped in a fractured hydrogarnet (H-adr)
846 (modified from Ménez et al. (2012) with permission). The orange dashed lines show the locations
847 where two FIB foils (shown in Fig. 9) were milled. (b) and (c): associated elemental distributions of
848 magnesium (green), calcium (red), manganese (purple) and cobalt (blue). Mn and Co appear
849 selectively enriched in two distinct regions of the carbon-rich felt filling H-adr cracks. (d)
850 corresponding SEM-EDXS spectrum. Collection point is located by a white star in (c). Pt and Au
851 arise from the metallic coating.

852

853 **Fig. 9.** Electron microscopy images of the metal-bearing felt collected on the FIB foil milled in the
854 area enriched in Co [(a) and (b)] and on the FIB foil milled in the Mn-enriched region [(c) and (d)]
855 and associated STEM characterizations [from (e) to (h)] (see Fig. 8a for milling locations). (a) SEM
856 image of the FIB foil milled in the Co-enriched area. It shows a thin layer of felt interfacing an
857 andraditic hydrogarnet (H-adr) and the FIB foil protective layer of platinum. (b) associated TEM
858 images whose location is shown in (a). An enlarged view is shown in Fig. 10a. It shows black dots
859 spotting the carbon gel enclosing polyhedral serpentine (pol-spt) and well-crystallized serpentine.
860 (c) SEM image of the FIB foil milled in the Mn-enriched region showing felt enclosed within a
861 fractured H-adr. (d) associated TEM images showing numerous pol-spt enclosed in a C-rich porous
862 gel. An enlarged view is shown in Fig. 10c and in Supplementary Fig. 3. From (e) to (h): associated
863 HAADF-STEM images and corresponding STEM-EDXS elemental distributions. Locations of
864 (e)+(f) and (g)+(h) are shown using white squares in (b) and (c), respectively.

865

866 **Fig. 10.** Magnified TEM and STEM images of the metal-bearing felt collected on the FIB foil
867 milled in the area enriched in Co [(a) and (b)] and on the FIB foil milled in the Mn-enriched region
868 [from (c) to (h)] (Fig. 8a). Locations of (a) and (c) are indicated in Figs. 9b and 9d, respectively. (a)
869 nanometric Co-oxides dispersed in the organic gel around a well-crystallized serpentine (spt)
870 presenting non crystalline Mg- and C-bearing inclusion (Mg-C incl.). (b) associated HR-TEM
871 image showing Co-oxides. (c) polyhedral serpentine (pol-spt) spheroid contoured by a crust of Mn
872 and Fe close to an iron oxide (Fe-ox). (d) is a magnified view of (c) with location indicated by an
873 orange star in (c). In (b) and (d), atom plane fringes attest for the presence of well-defined
874 crystallographic planes (white arrows). (e) larger HAADF-STEM image of the encrusted pol-spt.
875 Location of (c) is shown by a white square. From (f) to (h): STEM-EDXS elemental images
876 showing the distribution of Fe (f), Mn (g) and Co (h). They show Co homogeneously distributed
877 outside the pol-spt in both the C-bearing phase and the Fe-ox whereas Fe and, to a lesser extent, Mn
878 are enriched in the metallic crust contouring some of the pol-spt. Associated STEM-EDXS spectra
879 are shown in Fig. 11.

880

881 **Fig. 11.** TEM-EDXS spectra associated with (1) the polyhedral serpentine (pol-spt), (2) the Mn/Fe
882 crust formed around the pol-spt shown in Figs. 10c-h, (3) the nanometric Co-oxides shown in Figs.
883 10a-b, (4) the carbon matrix found in the felt. Cu X-ray peak at 8 keV arises from the TEM grid.

884

885 **Fig. 12.** STXM characterization of the metal-bearing felt enclosed in a fractured hydrogarnet.
886 Analysis have been performed on the FIB foil displayed in Fig. 9c with associated TEM and
887 STEM-EDXS characterizations shown in Fig. 9d and Figs. 9g-h, respectively. (a) composite STXM
888 map showing the distribution of the Co- and Mn/Fe-bearing organic components contained in the
889 felt and appearing respectively in blue and green. The red colour figures the location of the silicate
890 component. (b) composite STEM-EDXS elemental image showing the distribution of Mg (red), Mn

891 (green) and Co (blue) in the area indicated by a white square in (a), as also shown in Fig. 9h. (c) C-
892 XANES spectra associated with the Co-bearing area and the Mn-enriched felt. It shows the
893 presence of aromatic or olefinic carbon (285.1 eV), aliphatic carbon (287.7 eV), and carboxyl
894 functional groups (288.6 eV). The peak at 290.4 eV can be related to carboxyl groups bounded to
895 metals.

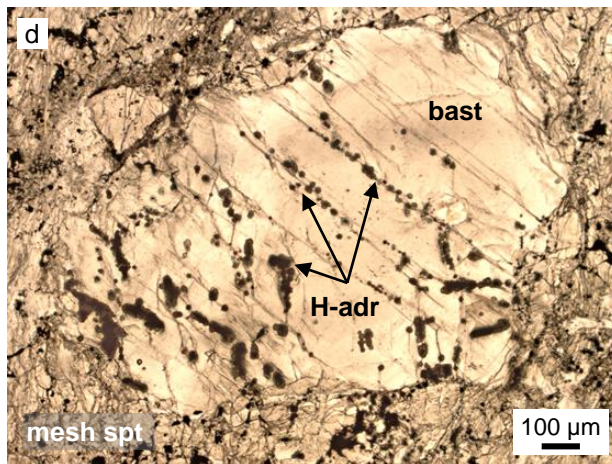
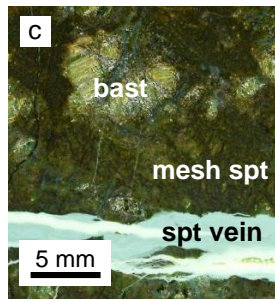
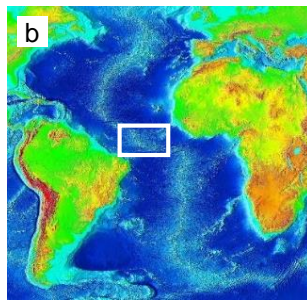
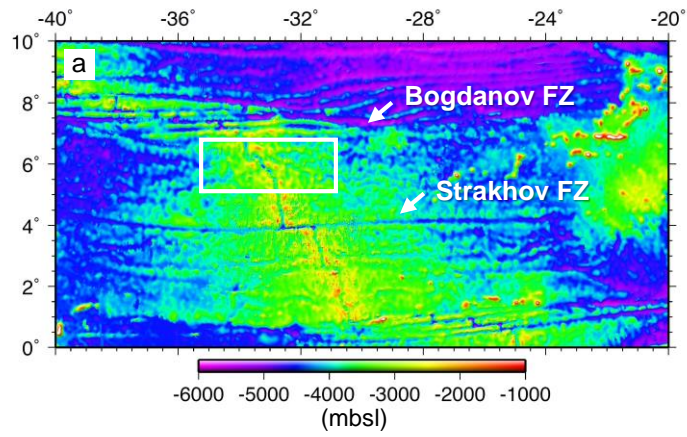
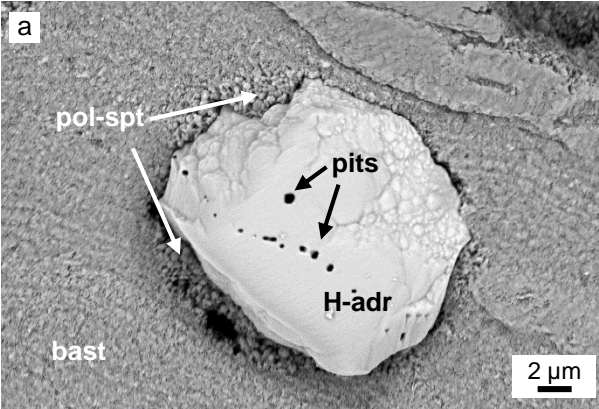
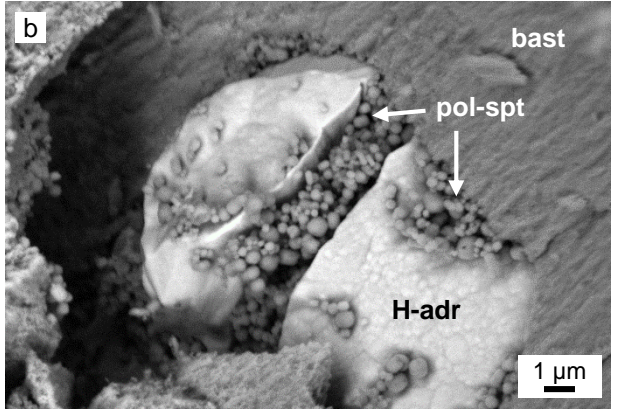


Figure 1 – Ménez et al.

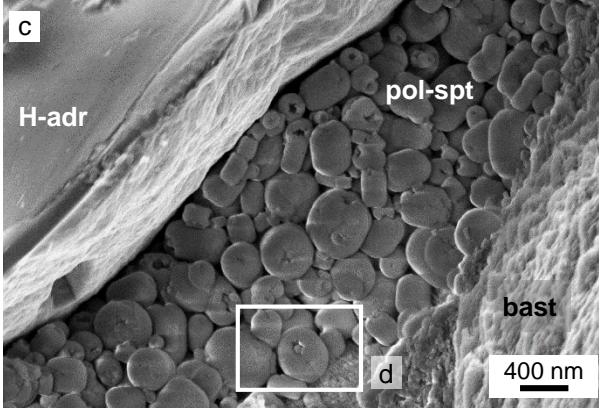
7 kV, backscattered electrons



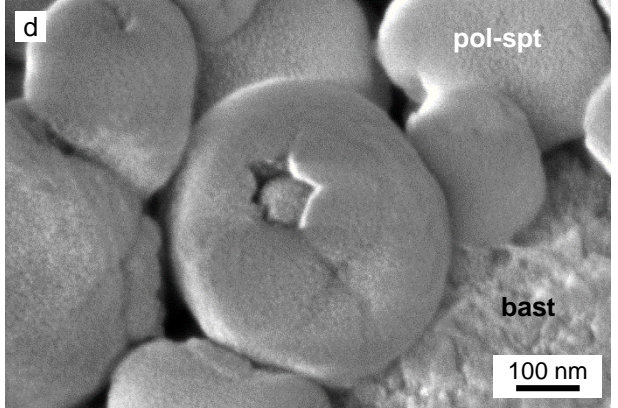
7 kV, backscattered electrons



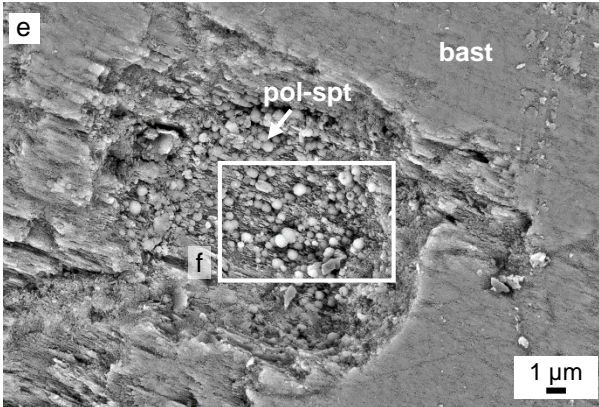
3 kV, secondary electrons



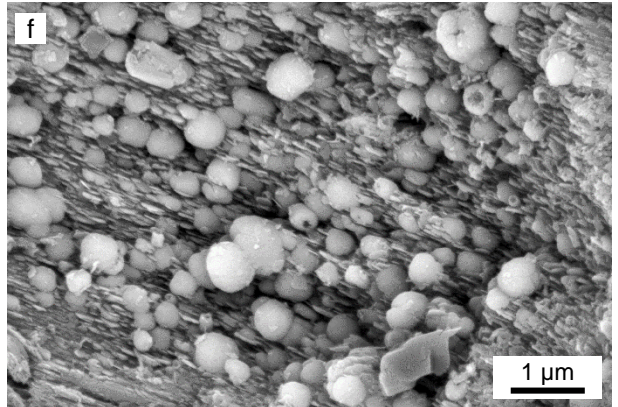
3 kV, secondary electrons



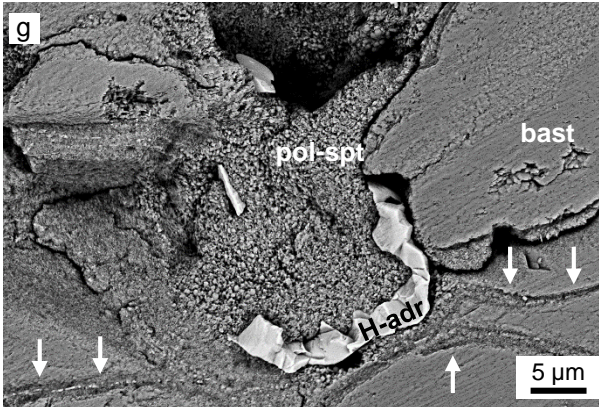
10 kV, backscattered electrons



10 kV, backscattered electrons



7 kV, backscattered electrons



10 kV, backscattered electrons

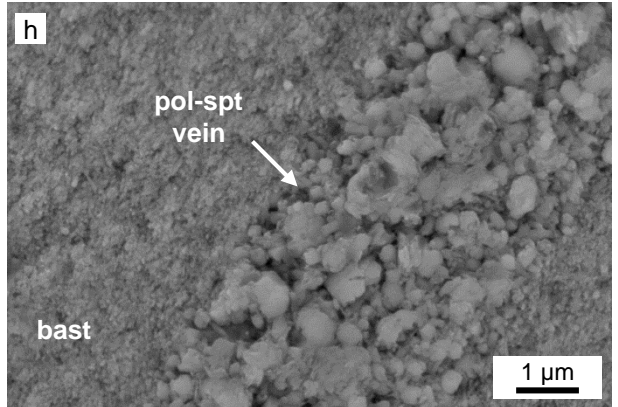


Figure 2 – Ménez et al.

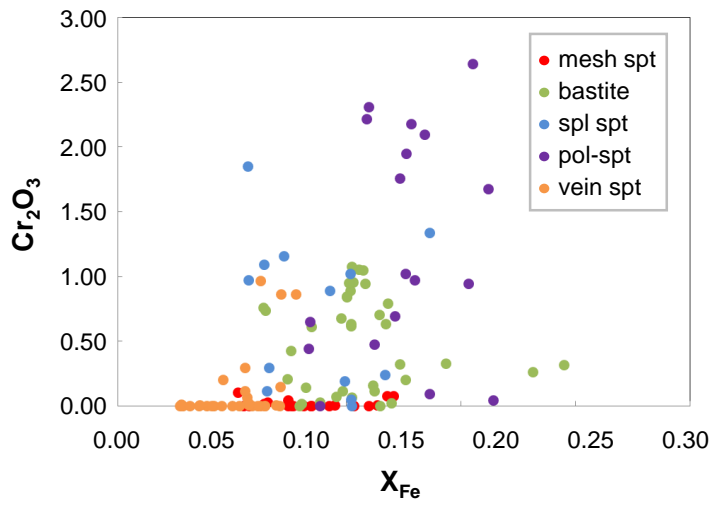


Figure 3 – Ménez et al.

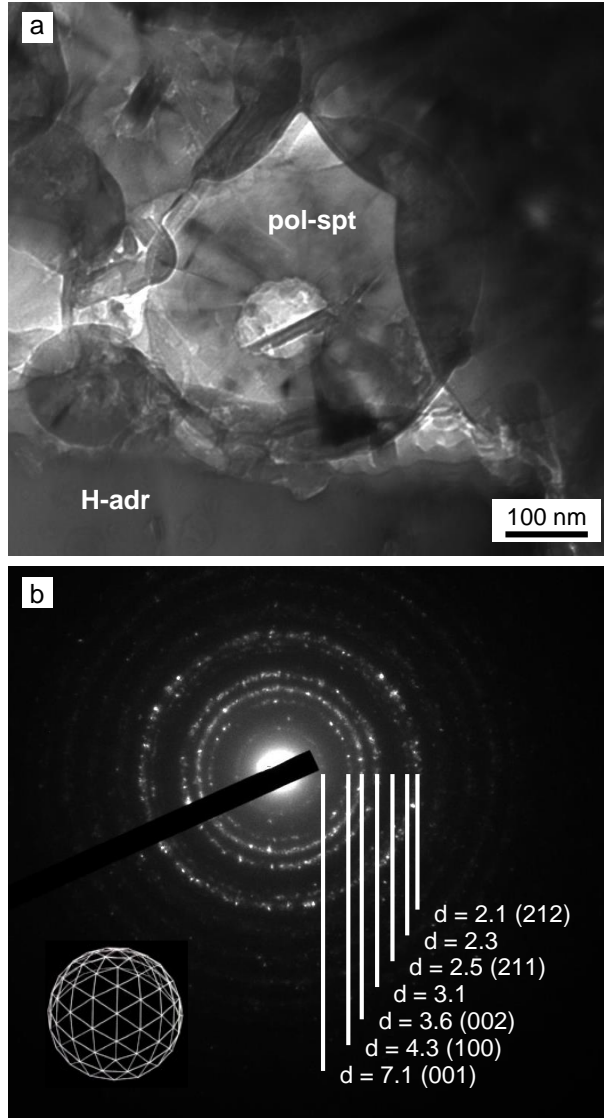
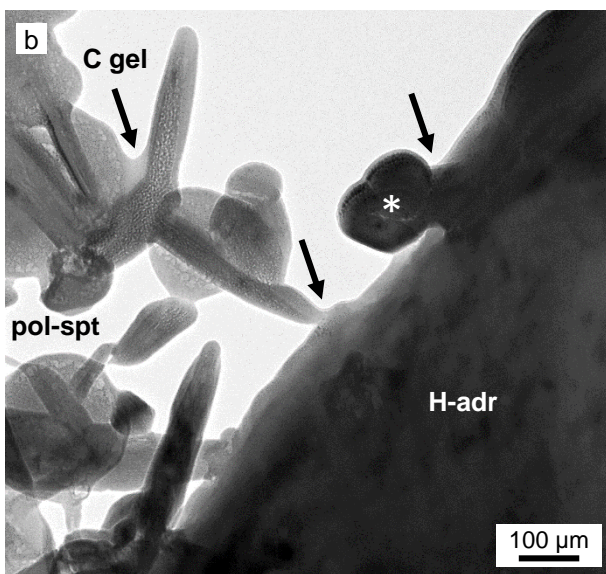
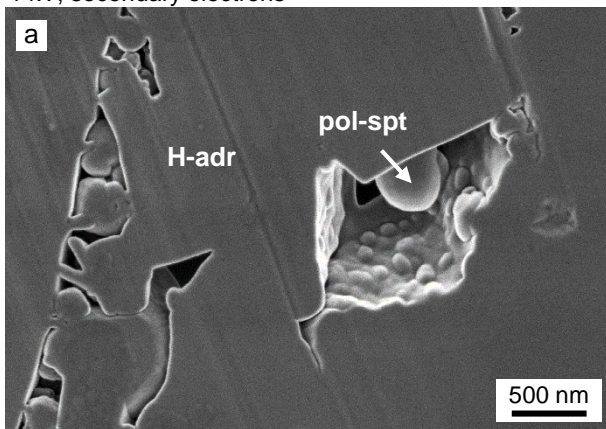


Figure 4 – Ménez et al.

1 kV, secondary electrons



15 kV, backscattered electrons

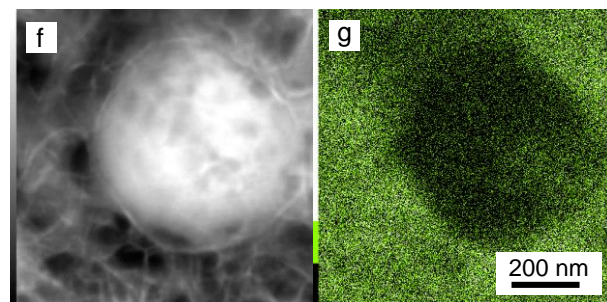
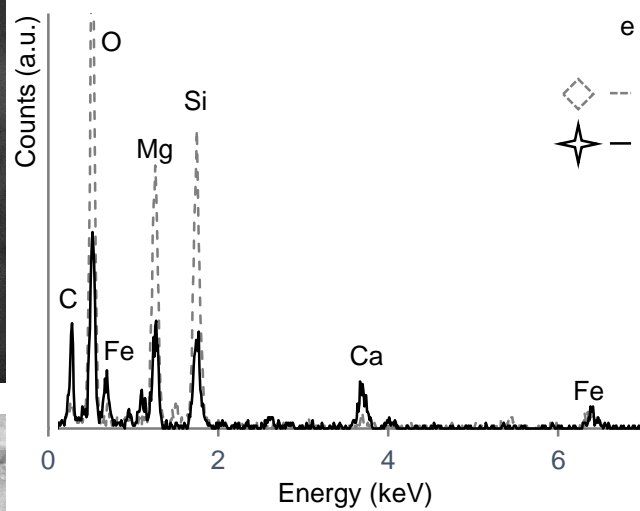
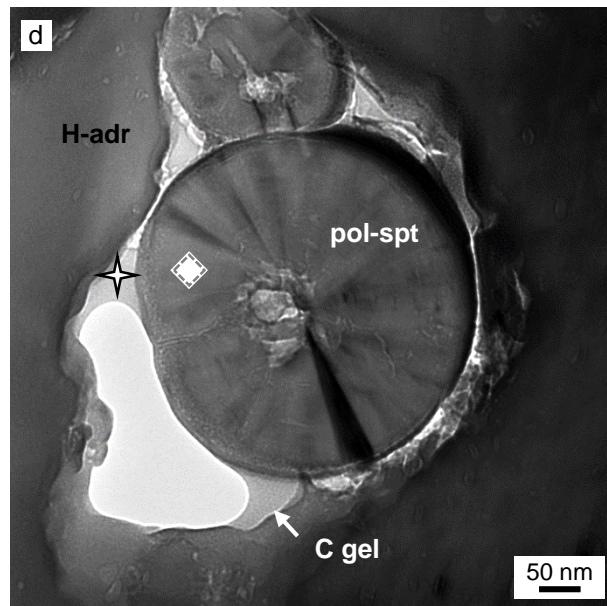
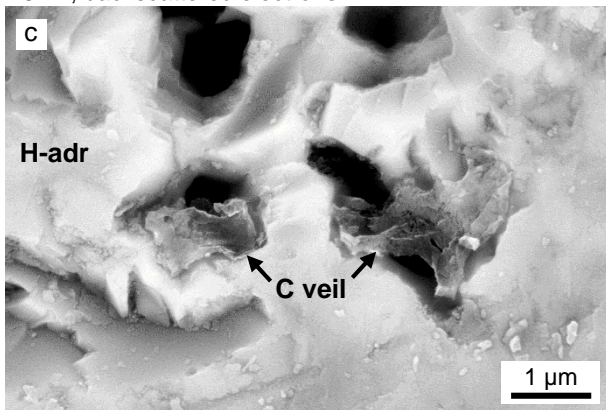
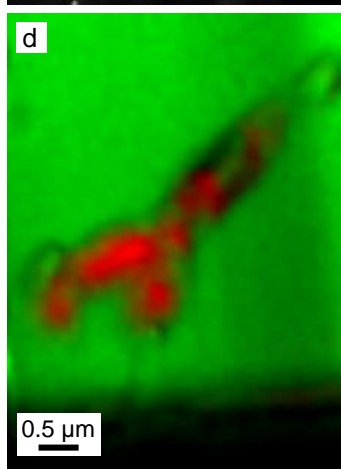
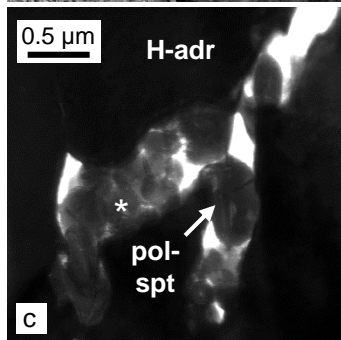
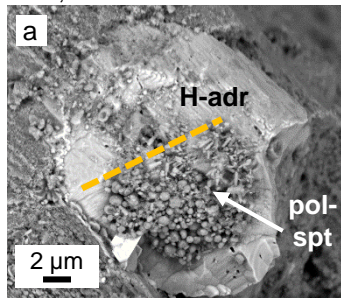


Figure 5 – Ménez et al.

7 kV, backscattered electrons



3 kV, secondary electrons

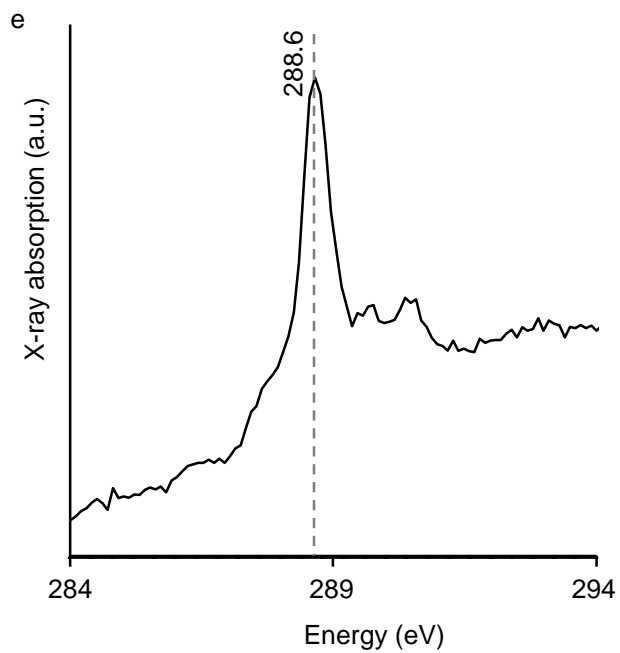
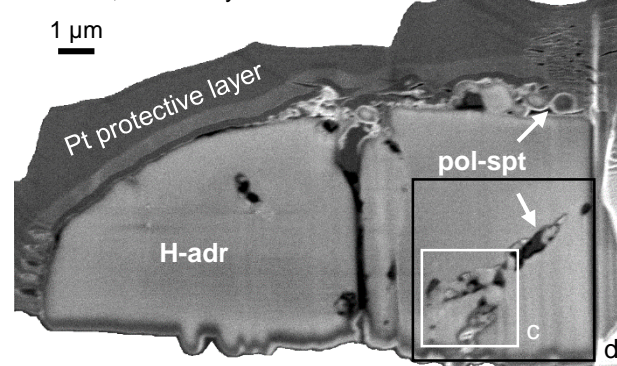
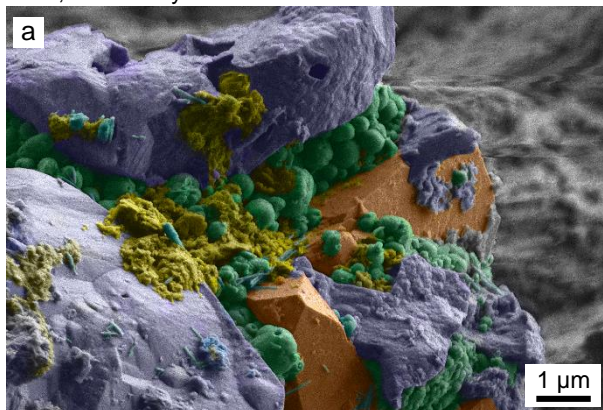
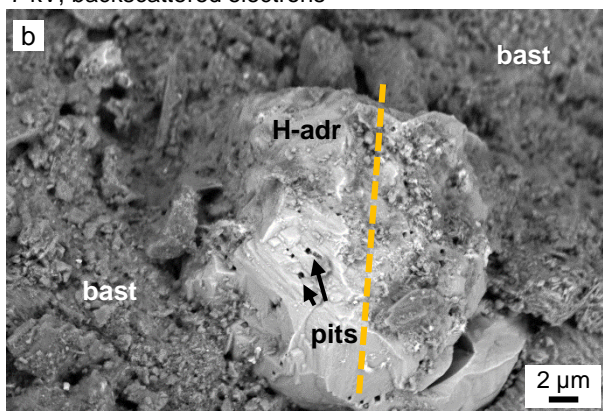


Figure 6 – Ménez et al.

2 kV, secondary electrons



7 kV, backscattered electrons



3 kV, secondary electrons

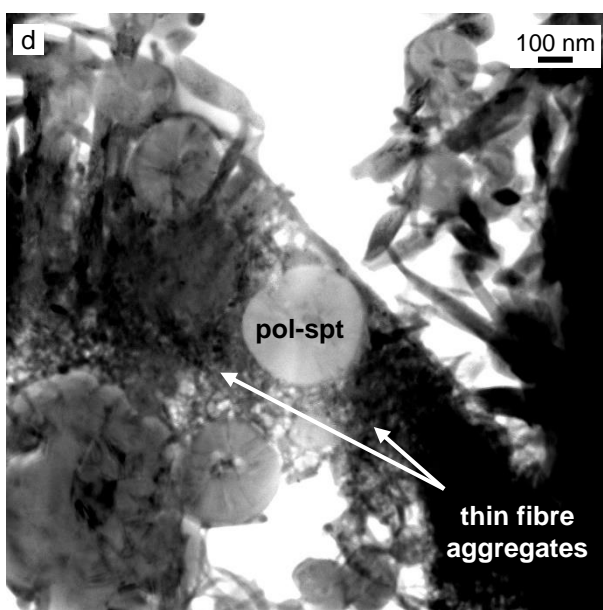
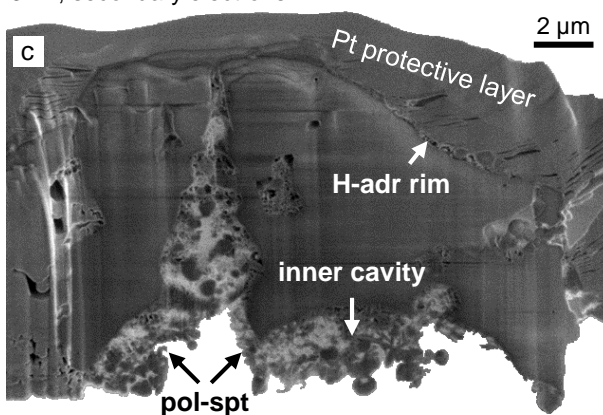


Figure 7 – Ménez et al.

10 kV, backscattered electrons

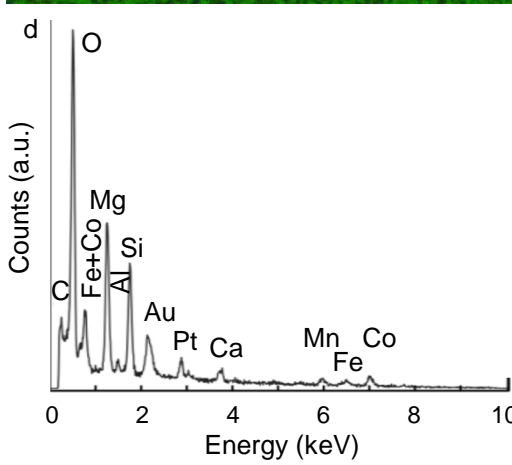
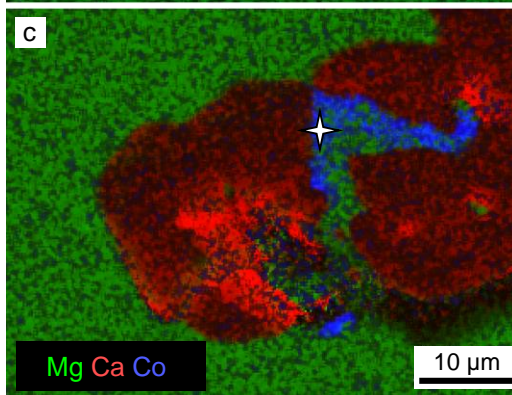
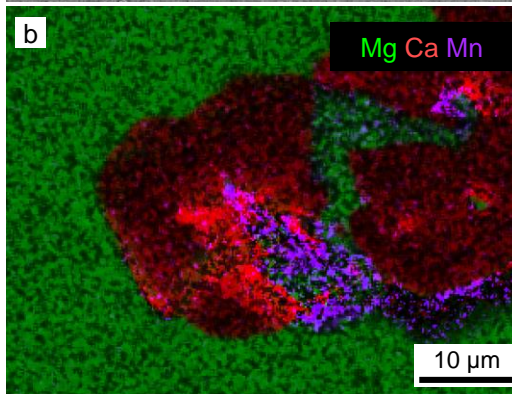
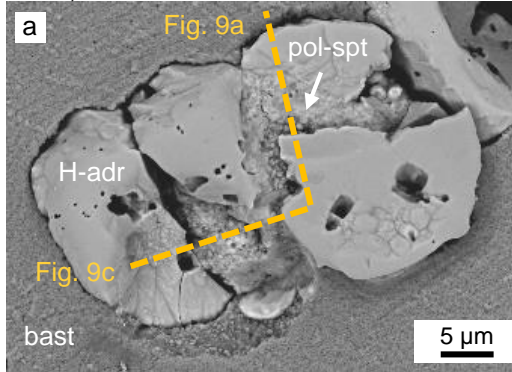


Figure 8 – Ménez et al.

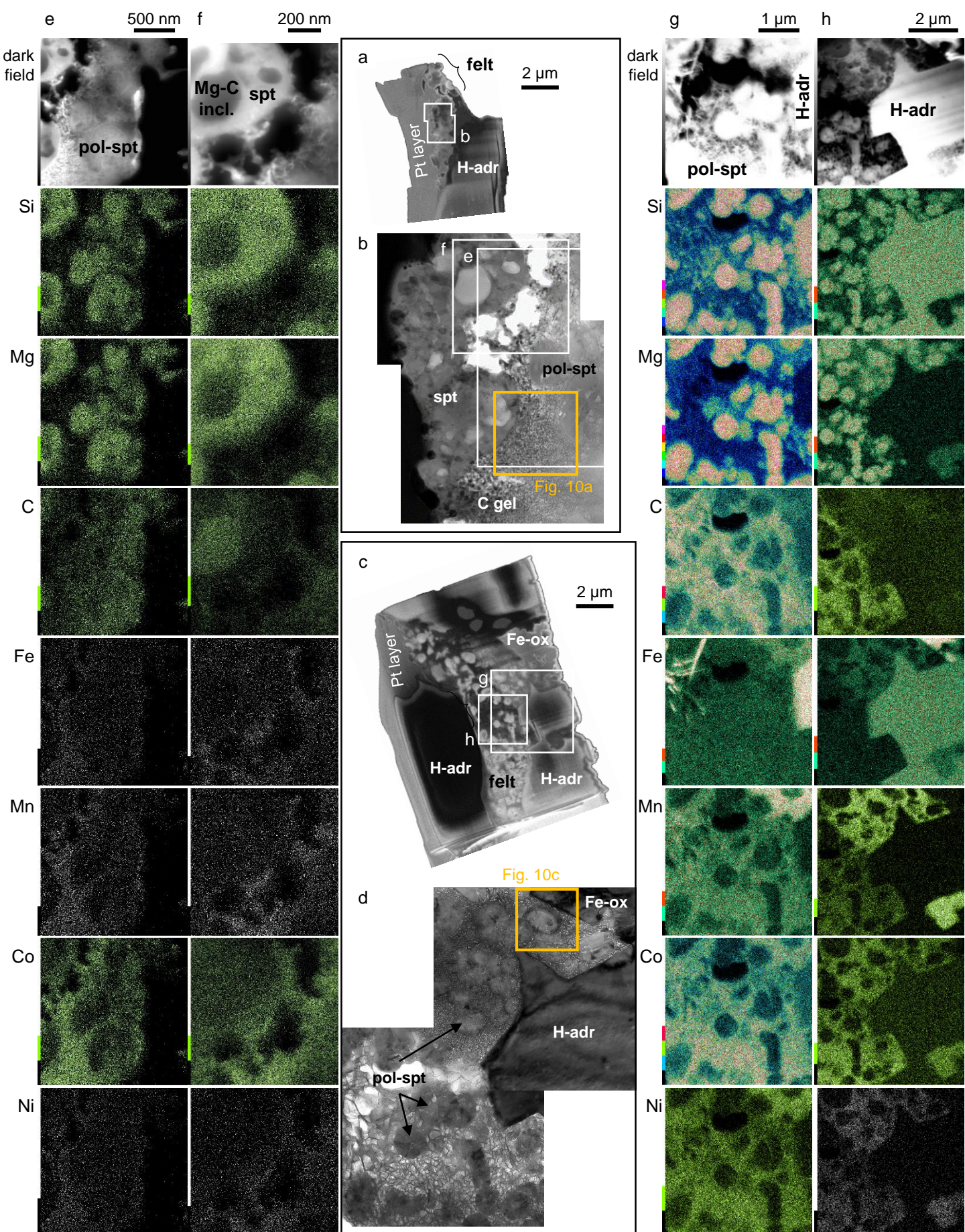


Figure 9 – Ménez et al.

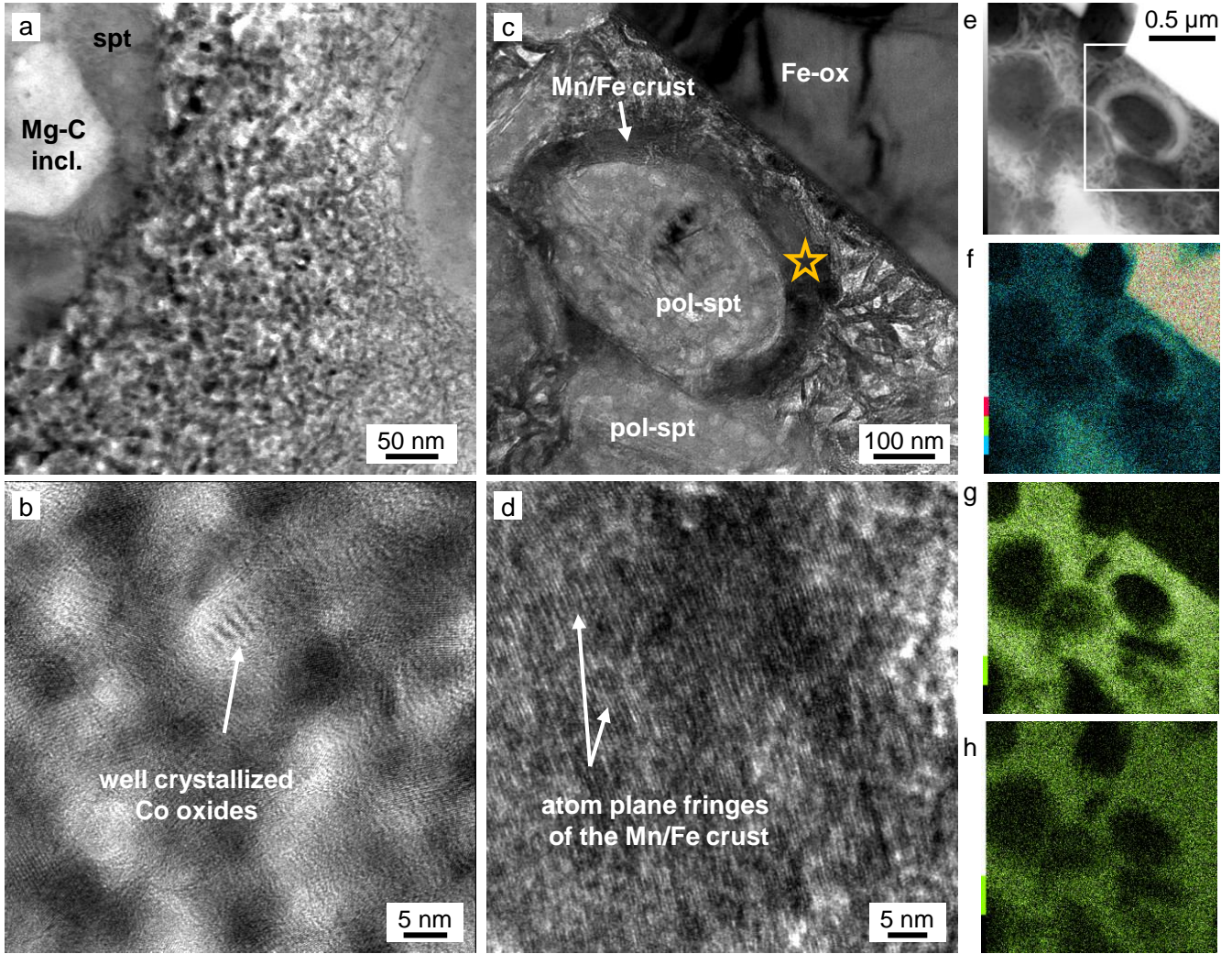


Figure 10 – Ménez et al.

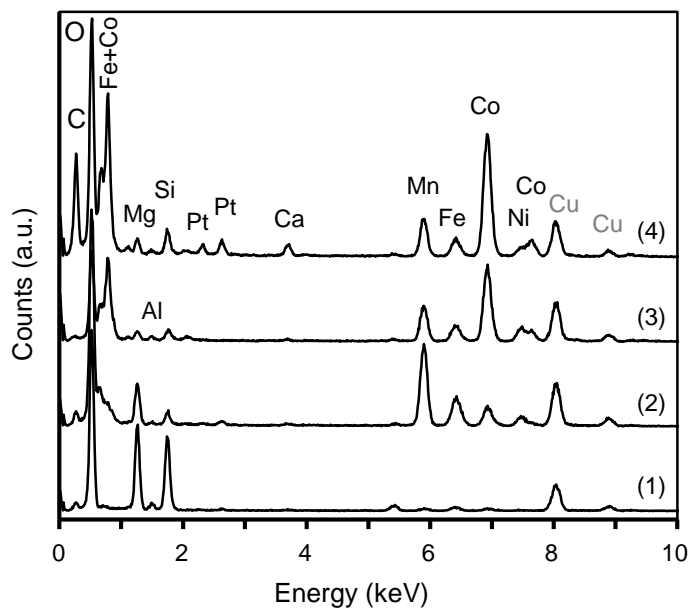


Figure 11 – Ménez et al.

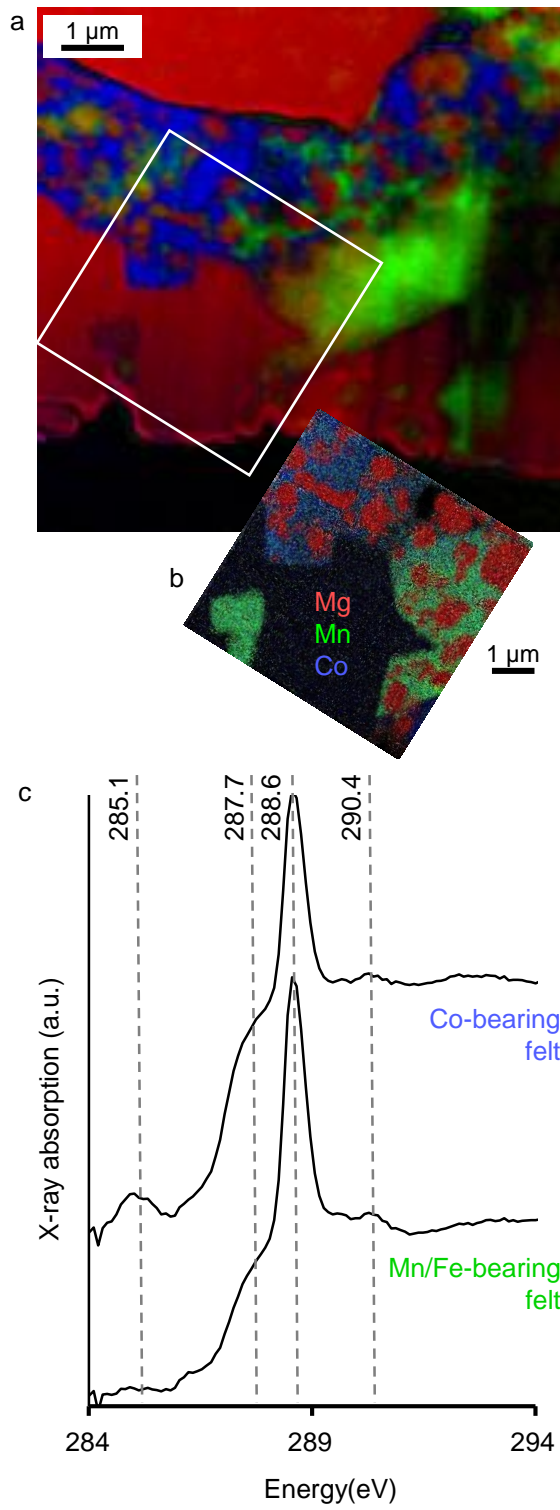


Figure 12 – Ménez et al.

